ribbon synapse. J Membr Biol 209 : 153-165, 2006

17) Khimich D, et al : Hair cell synaptic ribbons are essential for synchronous auditory signalling. Nature 434 : 889-894, 2005

18) Schmitz F, et al : RIBEYE, a component of synaptic ribbons : a protein's journey through evolution provides insight into synaptic ribbon function. Neuron 28 : 857-872, 2000

19) Grant L, et al : Calcium- and calmodulin-dependent inactivation of calcium channels in inner hair cells of the rat cochlea. J Neurophysiol 99 : 2183-2192, 2008

20) Johnson SL, et al : Biophysical properties of CaV1.3 calcium channels in gerbil inner hair cells. J Physiol 586 : 1029-1042, 2008

21) Bortolozzi M, et al : Calcium microdomains at presynaptic active zones of vertebrate hair cells unmasked by stochastic deconvolution. Cell Calcium 44 : 158-168, 2008

22) Roux I, et al : Otoferlin, defective in a human deafness form, is essential for exocytosis at the auditory ribbon synapse. Cell 127 : 277-289, 2006

23) Brandt N, et al : Thyroid hormone deficiency affects postnatal spiking activity and expression of Ca2+and K+channels in rodent inner hair cells. J Neurosci 27 : 3174-3186, 2007

24) Beutner D, et al : Calcium dependence of exocytosis and endocytosis at the cochlear inner hair cell afferent synapse. Neuron 29 : 681-690, 2001

25) Wittig JH, et al : Synaptic ribbon enables temporal precision of hair cell afferent synapse by increasing the number of readily releasable vesicles : a modeling study. J Neurophysiol 100 : 1724-1739, 2008

26) Griesinger CB, et al : Fast vesicle replenishment allows indefatigable signalling at the first auditory synapse. Nature 435 : 212-215, 2005

27) Goutman JD, et al : Time course and calcium dependence of transmitter release at a single ribbon synapse. Proc Natl Acad Sci U S A 104 : 16341-16346, 2007

28) Seal RP, et al : Sensorineural deafness and seizures in mice lacking vesicular glutamate transporter 3. Neuron 57 : 263-275, 2008

29) Glowatzki E, et al : Transmitter release at the hair cell ribbon synapse. Nat Neurosci 5 : 147-154, 2002

30) Chen Z, et al : Auditory sensitivity regulation via rapid changes in expression of surface AMPA receptors. Nat Neurosci 10 : 1238-1240, 2007

31) Ruel J, et al : Salicylate enables cochlear arachidonic-acid-sensitive NMDA receptor responses. J Neurosci 28 : 7313-7323, 2008

32) Puel JL, et al : Salicylate-induced tinnitus : molecular mechanisms and modulation by anxiety. Prog Brain Res 166 : 141-146, 2007

Clinical
Neuroscience

月刊 臨床神経科学

最新の治療デバイス

2011 Vol.29 4

中外医学社
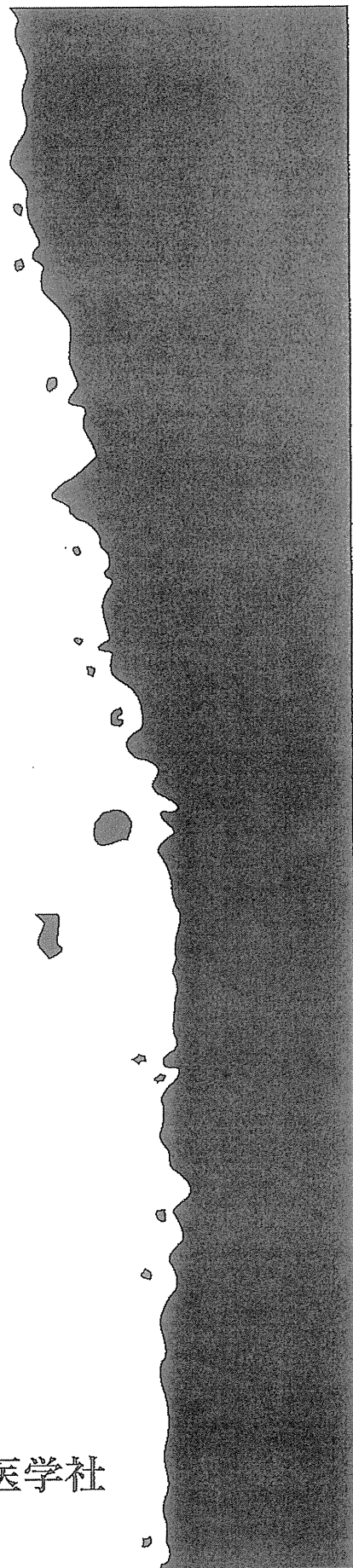
人工内耳

樫尾 明憲　山岨 達也

はじめに

平成 18 年度厚生労働省の報告で本邦における聴覚障害者の人数は 27 万人にのぼるといわれ，先天性高度難聴児の出生割合も 1000 人に 1 人と報告されており，高度難聴者の人数は決して少ない数字ではない[1]．補聴器は難聴の種類・程度によっては非常に有効な手段となるが，高度感音難聴者に対してはコミュニケーションに必要十分な聴覚補償が得られにくいというのが現実である．補聴器の装用効果がない高度難聴患者への新たな聴覚補助手段として，人工内耳は 1970 年代後半に開発，1980 年代より臨床応用が始まった[2]．本邦でも 1985 年より導入，1994 年には保険適用の認可がおり全国的に普及しつつある．人工内耳装用により，これまで補聴器では語音聴取がほとんど不可能となった中途失聴者が，人によっては携帯電話で会話ができるまで聴取能の回復を認めるようになった．また，先天性高度難聴児が人工内耳装用で療育次第では普通小学校へ通うことができるだけの口話コミュニケーション能力を獲得することも可能となった．本稿では人工内耳の原理，手術適応，問題点，将来展望について紹介する．

かしお あきのり　東京大学/耳鼻咽喉科
やまそば たつや　同 教授

聴覚と人工内耳

外界に存在する音は外耳道から進入し，鼓膜を振動させる．鼓膜の内側すなわち中耳に存在する耳小骨は鼓膜の振動を受けて，前庭窓より内耳へと振動を伝える．振動を受けた内耳は蝸牛内の基底板の振動をもたらし，蝸牛有毛細胞の聴毛と外膜にずれ運動が生じる．これにより有毛細胞の電気的発火がおこり，有毛細胞へ接続する神経線維，さらに，らせん神経節へと興奮が伝わり，電気的に音情報が中枢へと伝えられる（図1）．高度難聴の多くの原因は内耳の障害とされ，音振動が電気的刺激に変換できないことに起因する．人工内耳の原理は，内耳へ電極を挿入し，音信号に対応した電気的刺激を有毛細胞の代わりに直接神経へ伝えようというものである．蝸牛は 2.5 回転ある渦巻状の形状をなすが，基底部（基底回転）は高周波数の音感知を担い，頂上部（頂回転）は低周波数の音感知を行っている．人工内耳の蝸牛内に挿入される電極数は 12～22 個とメーカーにより異なるが，いずれの機種も基本的に外界の音の周波数分析を行い，それぞれに対応した神経線維，らせん神経節を刺激することでその情報を伝達し，音の強さは電流量により調節している．周波数の分析方法や電極の刺激
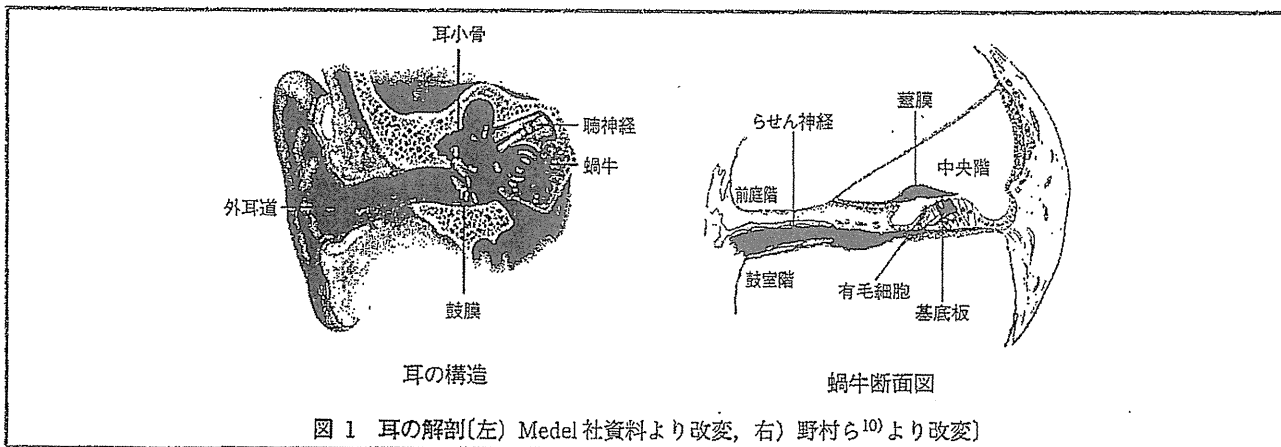

図 1　耳の解剖〔(左) Medel 社資料より改変，右) 野村ら[10]より改変〕

発生方法などはコード化法といい，各社で研究が進められて日々進歩している状況である．

人工内耳の適応

各国により若干異なった基準があるが，ここでは本邦における人工内耳の適応基準を紹介する．本邦では成人の場合(18歳以上)と小児の場合に分けて基準が作成されている．成人の場合は比較的単純で，要約すると，

① 原則両側90dB以上の高度難聴者で，かつ補聴器の装用効果がないもの

② 画像的所見で人工内耳挿入が可能であるもの

③ その他重篤な合併症がないもの

とされている．すなわち，人工内耳は補聴器の効果がない人が対象となり，補聴器装用で会話が可能な患者は人工内耳の適応とはなり得ない．一般的には補聴器装用下で単音節聴取能50%以下が適応といえる．重篤な合併症とは活動性中耳炎，重度の精神障害，聴覚中枢の障害などである．小児の場合は少々複雑で，抜粋すると，

① 術前から術後の療育に至るまで，家族および医療施設内外の専門職種との一貫した協力体制がとれている．

② 原則1歳6ヵ月以上

③ 原則両側90dB以上の高度難聴者で，6ヵ月以上の補聴器装用で言語獲得に必要な補聴効果が得られないと予想されるもの

④ 活動性中耳炎がないこと

とされている．成人例と異なりその多くは言語獲得期以前からの難聴があるため，人工内耳の目的は言語獲得となる．言語獲得を成し遂げるためには，人工内耳挿入後のハビリテーションが重要な役割を果たす．このためには乳幼児の聴覚障害に熟知している医療者，難聴者に対する言語聴覚コミュニケーション指導の可能な療育機関，そして言語獲得に向けての家族の一致団結した取り組みが適応の大前提となってくる．このうえで初めて医学的な適応条件が含まれてくることになる．海外の報告でも早期年齢の手術が言語獲得に有利に働くとの結果が報告されている[3]とおり，早期の手術の重要性が認識されつつあり，本邦でも適応年齢が2006年に2歳から1歳6ヵ月に引き下げられた経緯がある．ただし，乳幼児の聴力を判断することは決して容易ではなく，高度難聴の診断には慎重を要するのも事実で
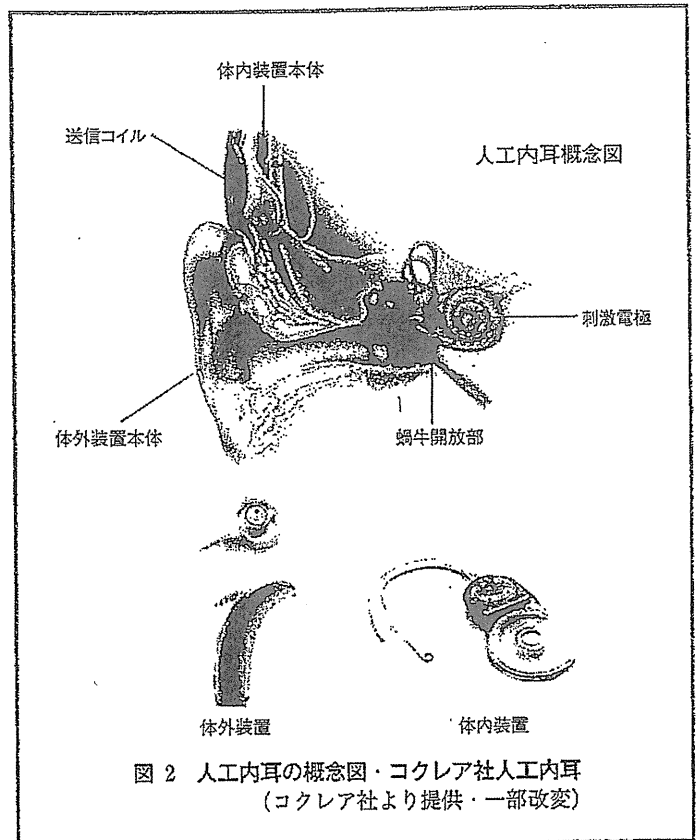

図2 人工内耳の概念図・コクレア社人工内耳
（コクレア社より提供・一部改変）

ある．この意味でも専門的な医療機関での聴力評価，6ヵ月以上にわたる補聴器装用・療育などによる言語発達の経過観察期間が極めて重要な意味を持ってくる．活動性中耳炎，または反復性中耳炎は術後人工内耳感染・髄膜炎などのリスクがあるため，適応は慎重に行う必要がある．画像所見で人工内耳挿入のスペースの確認できない場合や高度内耳奇形症例は，禁忌ではないが慎重な判断が求められる．内耳奇形があっても，蝸牛不全分離や前庭水管拡大症などの軽度の奇形の場合，成績は比較的良好である．一方，内耳道狭窄や蝸牛低形成など高度の奇形を伴うものではその成績は不良である[4]．また，重複障害・中枢性聴覚障害も禁忌とはされていないが，言語獲得の面ではその効果は限定的にならざるを得ない．このような症例では，人工内耳の効果の限界につき，家族にもそのエンドポイントを理解してもらったうえで手術適応を決定することが必要である．

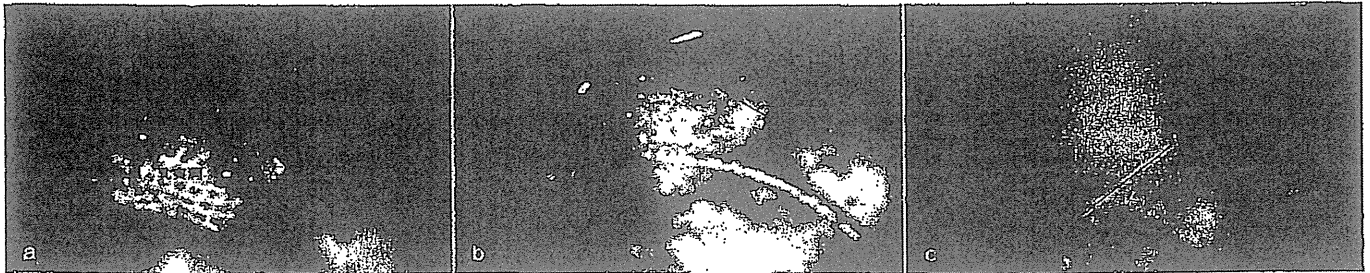## 人工内耳手術の実際

人工内耳は外界の音を収集し周波数分析を行い電気的信号に変換する体外装置，および体外装置より得た信号を電

図 3 人工内耳手術
a) 顔面神経窩を開放後，蝸牛を開放した．b) コクレア社 Nucleus Freedom CA 人工内耳挿入．
c) 術後頭部単純 X 線にて蝸牛内に人工内耳が挿入されていることを確認した．

極を通じて蝸牛内で発信する体内装置に分けられる（図2）．体外装置は補聴器と同様に耳介に装着し，後頭部の体外部送信コイルより，分析・変換した電気的信号を体内装置へ電磁波として伝達する．電磁波を受け蝸牛内へ電気的刺激を伝達する役割を果たす体内装置は手術的に頭部および蝸牛内へ埋め込む必要がある．体内装置の本体は通常耳介後上方の皮下に固定する．電極は側頭骨の乳突部削開を行い，顔面神経窩を開放して鼓室内へ通路を設け，蝸牛の鼓室階に挿入するのが一般的である（図 3 a，b）．人工内耳手術では蝸牛を開放し，電極を挿入するという侵襲的な操作を加えるため，基本的に残存聴力は消失しやすい．また，その影響が前庭に及び，術後眩暈をきたすこともある．鼓室への到達経路である顔面神経窩を開放する際は顔面神経および鼓索神経の約 2 mm 程度の間隙部分を削開する必要があり，両神経の損傷リスクが生じる．ただし，顔面神経については術中にモニタリングを行い確認するため頻度は極めて少ない．創部感染は術直後にも期間をあけても生じることもあり，常に気をつけなければならない．感染が悪化し人工内耳に感染が及ぶと，最悪の場合は本体の露出につながり摘出が必要となるため，早期の対応が重要となる．高度内耳奇形の場合，内リンパの脳脊髄液との交通が広い場合があり，その場合蝸牛開放の際に脳脊髄液の噴出（cerebro-spinal fluid gusher）を生じることがある．また，内耳奇形，および耳硬化症などによる蝸牛の脱灰が強い場合，誤挿入をきたすことが稀に存在する．術後 X 線・CT などで挿入位置を確認することが重要である（図 3 c）．内耳奇形や蝸牛脱灰症例では加えて，電極の刺激が顔面神経へ伝達されてしまう場合があり，その場合，音入力に対して顔面が痙攣することがおこりうる．通常電極の刺激方法を変更することで対応が可能であるが，時には不快感から人工内耳装用ができなくなることもある．

人工内耳の問題点

人工内耳は原理からも分かるとおり内耳障害による高度難聴に対してのみ有効である．聴神経腫瘍をはじめとした後迷路性難聴に対しては効果がない．また，失聴期間が長期に及ぶ場合，内耳性難聴であってもらせん神経節の変性が進むといわれ，その効果は限定的となる．人工内耳は術後すぐに言葉が話せると誤解されていることもあるが，術後，電極ごとに電流量・刺激方法の調整（マッピング）と（リ）ハビリテーションを行って初めて口話コミュニケーションが可能となってくる．特に，言語獲得期以前の失聴者の場合，言語獲得のための継続的なハビリテーションが不可欠であり，その環境整備ができなければ人工内耳の効果は十分望めないものと考えた方がよい．さらに，言語獲得には一般に臨界期というものが存在する（4〜5 歳）といわれ[5]，これを過ぎた場合では手術を行ったとしても環境音の認知は可能となりうるが，言語獲得はできない．それゆえ，先天性高度難聴患者の早期発見および早期診断が重要な問題として取り上げられ，新生児スクリーニング・乳幼児健診による難聴児の早期発見・早期療育が取り組まれているが，地域によっても格差が存在しまだ完全とはいえない状況である．なお，先天聾の成人患者に対しては，上記理由により基本的に人工内耳の適応はない．

人工内耳の装用効果は静寂下では語音聴取検査において正答率 80% 以上も可能であるが，騒音下における聴取は正常者に比べて極めて不良である．学校・会議中・街中をはじめとして，われわれの暮らす環境では騒音下での聴取が必要となる場所が多々あり，この点は今後改善されるべき問題として残っている．

最近の統計で人工内耳装用者の約5〜10%程度が機器の故障（外傷含む），感染などにより摘出・再手術を余儀なくされるという報告がある[6]．機器に起因する故障は各メーカーの取り組みでその率は年々少なくなっているが，感染・外傷などについては一定の率で発生する．特に小児は再手術により言語発達のブランクが生ずるので注意が必要である．

将来展望

各メーカーはディバイスの改良で故障率を少なくするよう努力している．MEL-EL社がホームページ上で報告している故障率は現行機種では6年間累積で純粋な機械トラブルが0.3%程度，外傷などの事故を含めると3.6%程度である．人工内耳の歴史はまだ浅く，長期的な成績については今後分かってくるものと思われ，特に外傷などの外的衝撃に起因する故障率も含めた安全性の向上には一層の注力が期待される．また，コード化法についても今後更なる進展が期待されよう．電極数はお互いの干渉の問題などもあり，単純に数を増やすことには限界があるようである．代わりに擬似的にチャンネル数を増加させるような試み[7]も行われている．また，低周波数について時間的情報も盛り込んでゆくという刺激方法（FSP：Fine Structure Processing）も登場[8]し，今後，言語聴取のみならず音楽などの聞き取り向上なども期待される．

本邦ではまだ保険適用にはなっていないが，海外では人工内耳を両側に適応することが既に始まっている．両側人工内耳の利点としては騒音下での聴取能の改善，音に対する方向感の獲得などがいわれている．コストベネフィットの問題，両側人工内耳を行うことで感染などのリスクが両側になる問題，再生医療など将来的な新たな治療に対する希望など，両側人工内耳を行ううえでいくつか問題はあるが，特に言語獲得期以前の小児に対しては言語獲得期に最大限の聴取能を獲得することが必要であり，今後適応拡大，普及が望まれるところである．

低音部に残聴がある患者に対して，通常よりも短い電極をより非侵襲的に挿入することで，低音部については補聴器などで補聴を行い，聴力の悪い高音部については人工内耳を活用しようというハイブリッド式（EAS：Electro-Acoustic Stimulation）の人工内耳も海外では実用化されつつある[9]．EASの登場で高音急墜型の感音難聴患者が人工内耳の恩恵を受けることができる可能性が出てきた．しかしながら，挿入後低音部の残聴が失われてしまう症例もあり，内耳機能をより確実に温存できる手術方法，ディバイスの改良が望まれるところである．

むすび

人工内耳は高度難聴者に対してする聴覚補償装置として画期的な成果を上げている．ただし，解決されるべき問題もあり，今後ハード・ソフト両面の進歩，および難聴者，特に小児に対する療育システムなどの発展が期待される．

文献
1) Estivill X, Fortina P, Surrey S, et al. Connexin-26 mutations in sporadic and inherited sensorineural deafness. Lancet. 1998；351：394-8.
2) 鈴木光也，山岨達也．人工臓器 最近の進歩．人工内耳．人工臓器．2009；38：155-8.
3) Niparko JK, Tobey EA, Thal DJ, et al. Spoken language development in children following cochlear implantation. JAMA. 2010；303：1498-506.
4) 坂井有紀，赤松裕介，尾形エリカ，他．小児内耳奇形に対する人工内耳埋込術と術後成績．Audiology Japan. 2008；51：633-40.
5) 池原由香，伊藤健，加我君孝．幼小児の難聴とCritical age—人工内耳手術から．加我君孝，編．中枢性聴覚障害の基礎と臨床．金原出版；2000.
6) 髙木明．人工内耳の最新知見 人工内耳手術と合併症の回避．JOHNS. 2008；24：1474-80.
7) Firszt JB, Holden LK, Reeder RM, et al. Speech recognition in cochlear implant recipients：comparison of standard HiRes and HiRes 120 sound processing. Otol Neurotol. 2009；30：146-52.
8) Lorens A, Zgoda M, Obrycka A, et al. Fine Structure Processing improves speech perception as well as objective and subjective benefits in pediatric MED-EL COMBI 40+ users. Int J Pediatr Otorhinolaryngol. 2010；74：1372-8.
9) Talbot KN, Hartley DE. Combined electro-acoustic stimulation：a beneficial union? Clin Otolaryngol. 2008；33：536-45.
10) 野村恭也，平出文久，原田勇彦．新耳科学アトラス—形態と計測値．シュプリンガー・フェアラーク東京；1992.

Carhart Notch 2-kHz Bone Conduction Threshold Dip

A Nondefinitive Predictor of Stapes Fixation in Conductive Hearing Loss With Normal Tympanic Membrane

Akinori Kashio, MD; Ken Ito, MD; Akinobu Kakigi, MD; Shotaro Karino, MD; Shin-ichi Iwasaki, MD; Takashi Sakamoto, MD; Takuya Yasui, MD; Mitsuya Suzuki, MD; Tatsuya Yamasoba, MD

Objective: To evaluate the significance of the Carhart notch (a 2-kHz bone conduction threshold dip [2KBD]) in the diagnosis of stapes fixation by comparing its incidence among ears with various ossicular chain abnormalities.

Design: Retrospective study.

Setting: University hospital.

Patients: A total of 153 ears among 127 consecutive patients with a congenital ossicular anomaly or otosclerosis.

Main Outcome Measures: The 2KBD depth was defined as the threshold at 2 kHz minus the mean of thresholds at 1 and 4 kHz. The presence of 2KBD (depth, ≥10 dB), 2KBD depth, relationship between 2KBD depth and air-bone gap, and 2-kHz bone conduction recovery after operation were evaluated in a stapes fixation group (which included cases of otosclerosis and congenital stapes fixation), an incudostapedial joint detachment group, and a malleus or incus fixation group.

Results: A 2KBD was present in 32 of 102 stapes fixation ears (31.4%), 5 of 19 incudostapedial joint detachment ears (26.3%), and 6 of 20 malleus or incus fixation ears (30.0%) (12 ears had other diagnoses). The mean (SD) 2KBD depths were 17.3 (5.2) dB in the stapes fixation group, 18.5 (2.2) dB in the incudostapedial joint detachment group, and 16.3 (2.1) dB in the malleus or incus fixation group. No statistically significant differences were noted among these 3 groups. No correlation was noted between 2KBD depth and air-bone gap extent. Recovery of 2-kHz bone conduction threshold in the stapes fixation group was less than that in the other 2 groups.

Conclusion: Incidence of 2KBD was similar among the stapes fixation, incudostapedial joint detachment, and malleus or incus fixation groups, implying that 2KBD is not a useful predictor of stapes fixation.

Arch Otolaryngol Head Neck Surg. 2011;137(3):236-240

Author Affiliations:
Department of Otolaryngology, Faculty of Medicine, University of Tokyo (Drs Kashio, Kakigi, Karino, Iwasaki, Sakamoto, Yasui, and Yamasoba), and Department of Otolaryngology, Teikyo University School of Medicine (Dr Ito), Tokyo, and Department of Otolaryngology–Head and Neck Surgery, Sakura Medical Center, University of Toho, Chiba (Dr Suzuki), Japan.

I N 1950, CARHART[1] REPORTED BONE conduction threshold elevation of approximately 2 kHz among patients with otosclerotic lesion–induced stapes ankylosis that disappeared after stapes surgery. Since then, this deceptive 2-kHz bone conduction threshold dip (2KBD) without inner ear damage has become a well-known indicator of stapes fixation (Carhart notch). However, results of studies[2-9] have suggested that elevation in bone conduction thresholds between 1 and 4 kHz can be caused by various factors that affect the conductive mechanism of the middle ear. In fact, it is not uncommon to encounter cases of Carhart notch in which hearing loss is caused by detachment of the incudostapedial joint. For Carhart notch to be used as a preoperative predictor of stapes fixation, it should be shown that the notch exists with stapes fixation but not with other ossicular chain disorders, such as disconnection; however, few clinical investigations have assessed this issue. In the present study, we evaluated the significance of 2KBD depth, defined as the threshold at 2 kHz minus the mean of thresholds at 1 and 4 kHz, in diagnosing various ossicular chain abnormalities in the setting of a normal tympanic membrane.

METHODS

We studied 153 ears among 127 consecutive patients who had a congenital ossicular anomaly or otosclerosis that was confirmed during surgery between January 1997 and December 2007 at the University of Tokyo Hospital, Tokyo, Japan. On the basis of the diagnosis made during surgery, we assigned these ears to the following 3 groups:

Table 1. Postoperative Diagnosis, Age, and Preoperative Air and Bone Conduction Thresholds Among Patients With the Various Pathologic Conditions

Postoperative Diagnosis	No. of Ears	Mean (SD)		
		Patient Age, y	ACT, dB	BCT, dB
Stapes fixation	102	48 (15)	58.3 (15.1)	26.3 (11.0)
Incudostapedial joint detachment	19	26 (17)	54.0 (11.9)	15.8 (7.0)
Malleus or incus fixation	20	24 (22)	56.8 (13.5)	19.2 (12.4)
Other	12	22 (16)	65.1 (8.4)	17.2 (12.5)

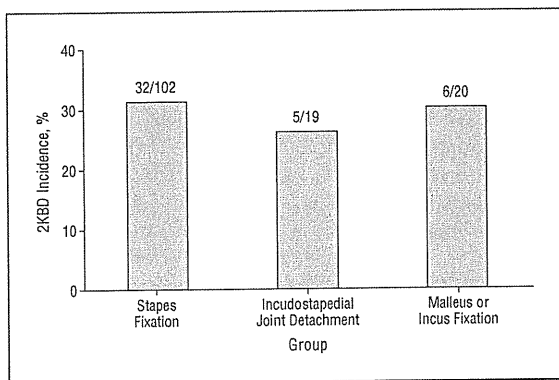Abbreviations: ACT, air conduction threshold; BCT, bone conduction threshold.

Figure 2. Depth of 2-kHz bone conduction threshold dip (2KBD) among various pathologic conditions. Error bars indicate standard error.

Figure 1. Incidence of 2-kHz bone conduction threshold dip (2KBD) among various pathologic conditions.

Table 2. Age-Related 2-kHz Bone Conduction Threshold Dip (2KBD)–Positive Rates

Age Group, y	Postoperative Diagnosis	No.	2KBD Positive
0-29	Stapes fixation	8	1
	Incudostapedial joint detachment	12	2
	Malleus or incus fixation	15	5
	Total, No. (%)	35	8 (22.9)
30-59	Stapes fixation	70	20
	Incudostapedial joint detachment	6	2
	Malleus or incus fixation	2	0
	Total, No. (%)	78	22 (28.2)
≥60	Stapes fixation	24	11
	Incudostapedial joint detachment	1	1
	Malleus or incus fixation	3	1
	Total, No. (%)	28	13 (46.4)

a stapes fixation group (which included cases of otosclerosis and congenital stapes fixation), an incudostapedial joint detachment group, and a malleus or incus fixation group. The medical records of these patients were retrospectively reviewed. Stapes fixation was observed in 102 ears (including 15 ears with congenital fixation), incudostapedial joint detachment without stapes fixation in 19 ears, and malleus or incus fixation without stapes fixation in 20 ears. The other 12 ears (including a combination of incudostapedial joint detachment and malleus or incus fixation or obstruction of the oval window) could not be classified into the aforelisted groups and were excluded from the analysis. The patients ranged in age from 6 to 72 years (mean [SD] age, 40 [20] years). Postoperative diagnoses and the mean age and mean preoperative air and bone conduction thresholds (at 0.5, 1, and 2 kHz) are given in Table 1. Patients in the stapes fixation group were significantly older than those in the other 2 groups. No significant differences were noted among the 3 groups in preoperative air or bone conduction thresholds.

For audiometric evaluation, we measured air conduction thresholds at 0.125, 0.25, 0.5, 1, 2, 4, and 8 kHz. Bone conduction thresholds were measured at 0.5, 1, 2, and 4 kHz. Pure-tone audiometry was performed more than once on various days before surgery. The 2KBD was considered present when the bone conduction threshold at 2 kHz exceeded the mean of thresholds at 1 and 4 kHz by at least 10 dB. The 2KBD depth was calculated by subtracting the mean of thresholds at 1 and 4 kHz from the bone conduction threshold at 2 kHz.

Values were recorded as the mean (SD) unless indicated otherwise. Statistical analyses used χ^2 test, Wilcoxon signed rank test, and 1-way analysis of variance with Bonferroni post hoc test.
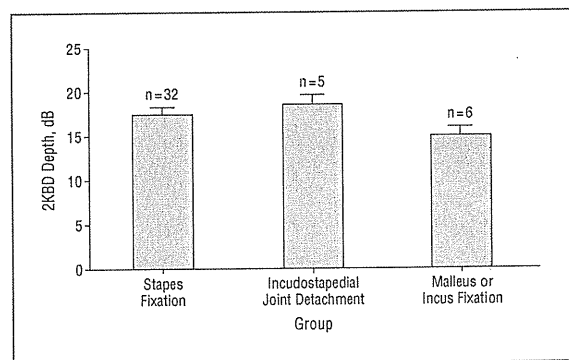
RESULTS

The 2KBD was detected in 32 of 102 ears (31.4%) in the stapes fixation group, 5 of 19 ears (26.3%) in the incudostapedial joint detachment group, and 6 of 20 ears (30.0%) in the malleus or incus fixation group (Figure 1). The mean 2KBD depths were 17.3 (5.2) dB in the stapes fixation group, 18.5 (2.2) dB in the incudostapedial joint detachment group, and 16.3 (2.1) dB in the malleus or incus fixation group (Figure 2). No statistically significant differences were noted in 2KBD incidence or 2KBD depth among the 3 groups.

Table 2 gives age-related dip-positive rates. There were no significant differences in percentages of dip-positive cases among the different age groups.

Figure 3 shows the relationship between 2KBD depth and air-bone gap, indicating no correlation between the 2 variables. No apparent differences were observed among the 3 groups.

Table 3 gives 2-kHz bone conduction thresholds before and after surgery, as well as improvements obtained by surgery. Of 102 ears in the stapes fixation group, 3 ears were excluded in which ossicular reconstruction could not be performed. Of 19 ears in the incudostapedial joint detachment group, 1 was excluded because the patient dropped out during the postoperative follow-up period. Improvement in 2-kHz
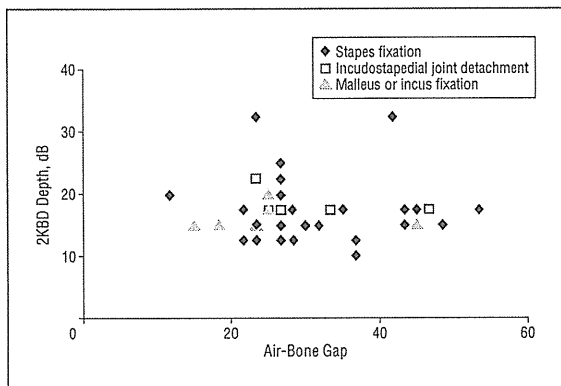
Figure 3. Relationship between 2-kHz bone conduction threshold dip (2KBD) depth and air-bone gap (r=0.34).
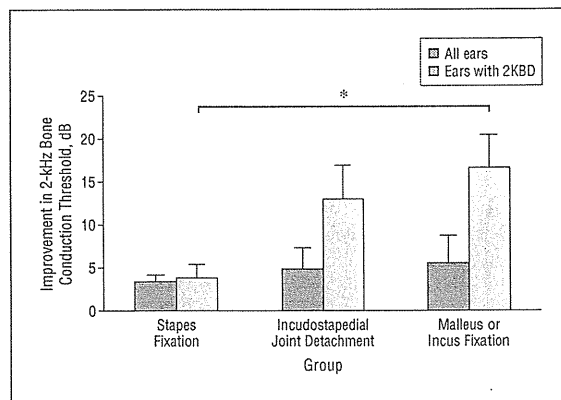

Figure 4. Postoperative recovery of 2-kHz bone conduction thresholds. Error bars indicate standard error, and the asterisk indicates a significant difference (P<.05, Bonferroni post hoc test). 2KBD indicates 2-kHz bone conduction threshold dip.

Table 3. Preoperative and Postoperative 2-kHz Bone Conduction Thresholds and Recovery

Postoperative Diagnosis	No. of Ears	2-kHz Bone Conduction Threshold, Mean (SD), dB		
		Preoperative	Postoperative	Recovery
Stapes fixation				
Total	99	35.0 (1.3)	31.2 (1.4)	4.6 (1.0)
2KBD positive	30	41.3 (2.0)	37.0 (2.8)	4.3 (1.9)
Incudostapedial joint detachment				
Total	18	22.2 (2.5)	16.9 (2.7)	5.6 (2.9)
2KBD positive	4	35.0 (5.3)	20.0 (6.2)	15.0 (4.7)
Malleus or incus fixation				
Total	20	26.5 (3.9)	20.1 (3.6)	6.3 (3.9)
2KBD positive	6	41.7 (7.8)	22.5 (7.7)	19.2 (4.6)

Abbreviation: 2KBD, 2-kHz bone conduction threshold dip.

bone conduction thresholds among the stapes fixation group was less than that among the other 2 groups; the difference between the 2KBD-positive stapes fixation group and the 2KBD-positive malleus or incus fixation group was statistically significant (P<.05, Bonferroni post hoc test) (**Figure 4**).

COMMENT

PREDICTIVE ABILITY OF CARHART NOTCH AND ITS UNDERLYING MECHANISMS

Acute or chronic otitis media associated with perforation of the tympanic membrane and otitis media with effusion can be diagnosed easily; however, in patients with normal tympanic membrane, sufficient information is needed to diagnose the cause of hearing loss. An audiological feature of 2KBD, Carhart notch, is widely known and is traditionally believed to suggest stapes fixation[10]; however, few investigations have verified its usefulness. In the present study, we evaluated the significance of Carhart notch in predicting stapes fixation and found that 2KBD was ineffective as a predictive tool. Incidence of Carhart notch was almost identical among the stapes fixa-

tion, incudostapedial joint detachment, and malleus or incus fixation groups. Otologic surgeons should be aware of this fact and should be ready to adapt their procedures according to pathologic findings during surgery.

Supporting our present findings that Carhart notch is not specific to stapes fixation, bone conduction threshold elevation between 1 and 4 kHz has also been reported in various pathologic conditions that affect the conductive mechanism of the middle ear. This phenomenon has been described in fluctuations of otitis media with effusion,[2,11-13] chronic otitis media,[5,6,14-17] experimental creation of artificial conductive impairment by loading the tympanic membrane,[8,18,19] occlusion of the round window or oval window,[8,9] and disarticulation of the incudostapedial joint.[9,20] Bone conduction threshold elevation has been reported principally between 1 and 4 kHz, with the largest being at 2 kHz.[2,5,7,21]

Bone conduction thresholds do not always represent a pure estimate of cochlear reserve, as many components are involved in bone conduction. The most important physical phenomena are believed to be (1) sound radiation into the ear canal, (2) inertial motion of the middle ear ossicles, and (3) compression and expansion of the bone encapsulating the cochlea.[22,23] Ossicular chain deficiencies are closely related to these components. A change in the ossicular chain may result in less inertial motion energy transmitted into the inner ear and can cause impedance mismatch between the inner ear and the ossicular system, modifying (decreasing or increasing) the loss of bone-conducted sound pressure from the vestibule to the footplate. It is reported that the middle ear does not contribute to perception of bone conduction sound at frequencies lower than 1 kHz.[8,20,24] At higher frequencies, the middle ear can affect bone conduction. Using human cadaver heads, Stenfelt[20] reported that motion of the stapes with bone conduction sounds was decreased by 5 to 10 dB between 1.2 and 2.7 kHz after the incudostapedial joint was severed. Using cats, Kirikae[8] reported a decrease in response at frequencies between 1 and 3 kHz after fixation of the stapes. With an intact ossicular chain, resonance frequency of the ossicular vibration with bone conduction stimulation is close to 1.5

kHz,[20] which explains 2-kHz bone conduction threshold elevation in ossicular deficiency. Therefore, although the underlying mechanisms may differ, 2-kHz bone conduction threshold elevation may well occur in various impairments of the ossicular chain, including stapes fixation, incudostapedial joint detachment, and malleus or incus fixation. The reason for this phenomenon seems complex, but oversimplification is inappropriate; further fundamental studies are needed to clarify its mechanism.

AGE-RELATED EFFECTS OF 2KBD

The mean age of patients in the stapes fixation group was significantly older than that of patients in the incudostapedial joint detachment group and the malleus or incus fixation group. In our cohort, patients in the latter 2 groups with normal tympanic membranes were mainly young adults or children with congenital malformations of the ossicular chain. This may explain the younger mean ages of these groups. Aging raises bone conduction thresholds at high frequencies, and elevation of 4-kHz bone conduction thresholds results in underestimation of potential 2KBD depths in older patients with stapes fixation. However, in our series, no significant differences were noted in 2KBD incidence among age groups. This suggests that age differences among the 3 study groups did not affect 2KBD incidence.

2KBD DEPTH AND 2-KHZ BONE CONDUCTION THRESHOLD RECOVERY AFTER SURGERY

Several investigations have focused on 2KBD, but its definitive criteria have not yet been established. However, previously reported mean 2KBD depths in otosclerosis ranged from 2.4 to 12.5 dB.[20,24,25] These studies included all cases and not just those classified as dip positive by certain criteria. The overall mean 2KBD depth, including dip-negative cases, was 8.5 dB in our stapes fixation group, which is within the range previously reported. For the 2KBD-positive cases, all 3 groups showed similar depths. These results suggest that an apparent elevation in bone conduction thresholds caused by a middle ear deficiency is similar regardless of the cause. Moreover, no correlation was observed between air-bone gap and 2KBD depth, suggesting that the depth may not be influenced by the degree of middle ear deficiency.

Carhart[1] originally reported postoperative bone conduction improvements of 5 dB at 500 Hz, 10 dB at 1 kHz, 15 dB at 2 kHz, and 5 dB at 4 kHz. Ginsberg et al[21] confirmed the finding of optimal bone conduction improvement at 2 kHz. Åwengen[25] showed an improvement of 4 to 12 dB for bone conduction at 2 kHz in otosclerosis after stapedectomy. In our series, the mean recovery of 2-kHz bone conduction was 4.6 to 6.3 dB, and the value was 4.3 to 19.2 dB when we limited the analysis to only dip-positive cases. Recovery trends in the stapes fixation group were worse than those in the other 2 groups. Gerard et al[26] proposed that there is less postoperative improvement in bone conduction with increasing age; this suggests that the aging cochlea is more susceptible to surgical damage. Because the mean age of patients was

significantly older in the stapes fixation group, this may have influenced their recovery. When we evaluated 33 younger patients (about one-third of the group; mean age, 33 years) from the stapes fixation group, the overall 2KBD recovery was 7.9 (1.8) dB, which was comparable to that of the other 2 groups. Surgical procedures used in stapes surgery are more invasive and involve opening of the inner ear. Cook et al[27] reported a weak ($r=0.28$) but significant ($P<.05$) correlation between bone conduction recovery at 2 kHz and air conduction recovery after stapes surgery. We also investigated this issue and found that bone conduction recovery at 2 kHz had a weak correlation with the mean air conduction recovery ($r=0.38$, $P<.05$) but observed that preoperative air-bone gap and 2-kHz bone conduction threshold recovery had no significant correlation ($r=-0.11$, $P>.05$). These facts imply that air and bone conduction threshold elevations are related somewhat but that the underlying mechanisms of these phenomena may not be simple.

REFERENCES

1. Carhart R. Clinical application of bone conduction audiometry. *Arch Otolaryngol.* 1950;51(6):798-808.
2. Yasan H. Predictive role of Carhart's notch in pre-operative assessment for middle-ear surgery. *J Laryngol Otol.* 2007;121(3):219-221.
3. Ahmad I, Pahor AL. Carhart's notch: a finding in otitis media with effusion. *Int J Pediatr Otorhinolaryngol.* 2002;64(2):165-170.
4. Conijn EA, Van der Drift JF, Brocaar MP, Van Zanten GA. Conductive hearing loss assessment in children with otitis media with effusion: a comparison of pure tone and BERA results. *Clin Otolaryngol Allied Sci.* 1989;14(2):115-120.
5. Browning GG, Gatehouse S. Hearing in chronic suppurative otitis media. *Ann Otol Rhinol Laryngol.* 1989;98(4, pt 1):245-250.
6. Dumich PS, Harner SG. Cochlear function in chronic otitis media. *Laryngoscope.* 1983;93(5):583-586.
7. Tüz M, Doğru H, Uygur K, Gedikli O. Improvement in bone conduction threshold after tympanoplasty. *Otolaryngol Head Neck Surg.* 2000;123(6):775-778.
8. Kirikae I. An experimental study on the fundamental mechanism of bone conduction. *Acta Otolaryngol Suppl.* 1959;145:1-111.
9. Tonndorf J, Campbell R, Bernstein L, Reneau JI. Quantitative evaluation of bone conduction components in cats. *Acta Otolaryngol Suppl.* 1966;213:10-38.

10. Lam HY. Causes of hearing disorders. In: Kerr AG, ed. *Scott-Brown's Otolaryngology Adult Audiology.* 6th ed. Oxford, England: Butterworth-Heinemann; 1996: 2.10.1-2.10.28.

11. Dirks DD. Bone-conduction testing. In: Katz J, ed. *Handbook of Clinical Audiology.* 3rd ed. Baltimore, MD: Williams & Wilkins; 1985.

12. Naunton RF, Fernandez C. Prolonged bone conducton: observations on man and animals. *Laryngoscope.* 1961;71:306-318.

13. Huizing EH. Bone conduction—the influence of the middle ear. *Acta Otolaryngol Suppl.* 1960;155:1-99.

14. Goodhill V. The fixed malleus syndrome. *Trans Am Acad Ophthalmol Otolaryngol.* 1966;70(3):370-380.

15. Dirks DD, Malmquist GM. Comparison of frontal and mastoid bone-conduction thresholds in various conductive lesions. *J Speech Hear Res.* 1969;12(4):725-746.

16. Priede V. Acoustic impedance in two cases of ossicular discontinuity. *Int Audiol.* 1970;1:127-136.

17. Linstrom CJ, Silverman CA, Rosen A, Meiteles LZ. Bone conduction impairment in chronic ear disease. *Ann Otol Rhinol Laryngol.* 2001;110(5 Pt 1):437-441.

18. Barany E. A contribution to the physiology of bone conduction. *Acta Otolaryngol Suppl.* 1938;26:1-223.

19. Allen GW, Fernandez C. The mechanism of bone conduction. *Ann Otol Rhinol Laryngol.* 1960;69:5-28.

20. Stenfelt S. Middle ear ossicles motion at hearing thresholds with air conduction and bone conduction stimulation. *J Acoust Soc Am.* 2006;119(5, pt 1):2848-2858.

21. Ginsberg IA, Hoffman SR, Stinziano GD, White TP. Stapedectomy—in depth analysis of 2405 cases. *Laryngoscope.* 1978;88(12):1999-2016.

22. Stenfelt S, Goode RL. Bone-conducted sound: physiological and clinical aspects. *Otol Neurotol.* 2005;26(6):1245-1261.

23. Stenfelt S. Bone-conduction hearing and the occlusion effect in otosclerosis and normal controls. *Otol Neurotol.* 2005;26(6): 1138-1142.

24. Moller AR. *Hearing: Its Physiology and Pathophysiology.* San Diego, CA: Academic Press; 2000.

25. Àwengen DF. Change of bone conduction thresholds by total footplate stapedectomy in relation to age. *Am J Otolaryngol.* 1993;14(2):105-110.

26. Gerard JM, Serry P, Gersdorff MC. Outcome and lack of prognostic factors in stapes surgery. *Otol Neurotol.* 2008;29(3):290-294.

27. Cook JA, Krishnan S, Fagan PA. Quantifying the Carhart effect in otosclerosis. *Clin Otolaryngol Allied Sci.* 1995;20(3):258-261.

Behavioral/Systems/Cognitive

Axonal Branching Patterns as Sources of Delay in the Mammalian Auditory Brainstem: A Re-Examination

Shotaro Karino,[1,4] Philip H. Smith,[2] Tom C. T. Yin,[3] and Philip X. Joris[1]

[1]Laboratory of Auditory Neurophysiology, Medical School, University of Leuven, B-3000 Leuven, Belgium, Departments of [2]Anatomy and [3]Physiology, University of Wisconsin–Madison, Madison, Wisconsin 53706-1510, and [4]Department of Otolaryngology, Faculty of Medicine, University of Tokyo, Tokyo 113-8655, Japan

In models of temporal processing, time delays incurred by axonal propagation of action potentials play a prominent role. A pre-eminent model of temporal processing in audition is the binaural model of Jeffress (1948), which has dominated theories regarding our acute sensitivity to interaural time differences (ITDs). In Jeffress' model, a binaural cell is maximally active when the ITD is compensated by an internal delay, which brings the inputs from left and right ears in coincidence, and which would arise from axonal branching patterns of monaural input fibers. By arranging these patterns in systematic and opposite ways for the ipsilateral and contralateral inputs, a range of length differences, and thereby of internal delays, is created so that the ITD is transformed into a spatial activation pattern along the binaural nucleus. We reanalyze single, labeled, and physiologically characterized axons of spherical bushy cells of the cat anteroventral cochlear nucleus, which project to binaural coincidence detectors in the medial superior olive (MSO). The reconstructions largely confirm the observations of two previous reports, but several features are observed that are inconsistent with Jeffress' model. We found that ipsilateral projections can also form a caudally directed delay line pattern, which would counteract delays incurred by caudally directed contralateral projections. Comparisons of estimated axonal delays with binaural physiological data indicate that the suggestive anatomical patterns cannot account for the frequency-dependent distribution of best delays in the cat. Surprisingly, the tonotopic distribution of the afferent endings indicate that low characteristic frequencies are under-represented rather than over-represented in the MSO.

Introduction

Coincidence detectors and time delays are common ingredients in models of temporal processing. In such models, neural equivalents of cross-correlation or autocorrelation are implemented by comparing spike trains with delayed versions of themselves or with other spike trains. A pre-eminent example is in binaural hearing, which affords the detection of minute time differences in the sound signals to the two ears [interaural time differences (ITDs)] that contain information about the spatial properties of sound sources. Neuronal ITD sensitivity in mammals originates in the medial superior olive (MSO). For >50 years, one model (Jeffress, 1948) has dominated the discussion of the neural mechanisms of ITD discrimination and its relationship to MSO activity. In this model, a binaural cell shows a "best delay": it is maximally active when the external acoustic delay (the ITD) is compensated by an internal delay, so that the inputs from left and right ear to the cell are coincident. Classic studies of ITD sensi-

tivity (Rose et al., 1966; Goldberg and Brown, 1969; Yin and Chan, 1990) provided evidence for coincidence in accord with the Jeffress (1948) model (Joris et al., 1998; Joris, 2006). Jeffress hypothesized the source of internal delays as axonal length differences. He proposed that afferent axons are systematically arranged with length gradients in opposite directions for ipsilateral (Ipsi) and contralateral (Contra) inputs to an array of coincidence detectors. The result would be a systematic gradation in best delay along the binaural nucleus and the conversion of ITDs into a spatial activation pattern along the array.

In mammals, only two studies have examined the existence of delay lines anatomically. Smith et al. (1993) physiologically characterized and then labeled single afferent axons to the MSO from spherical bushy cells of the anteroventral cochlear nucleus (AVCN). They concluded that the projections to the contralateral MSO, but not the ipsilateral MSO, display a rostrocaudal (RC) delay line configuration. Beckius et al. (1999) labeled small populations of AVCN neurons with an extracellular deposit, and selected and reconstructed individual axons. Their results were similar to those of Smith et al. (1993) with the additional finding of a length gradient running in the opposite (caudorostral) direction in some ipsilateral projections. Physiologically, MSO neurons show a rostrocaudal gradient in ITD tuning consistent with the anatomical predictions (Yin and Chan, 1990).

Despite the anatomical and physiological support, the Jeffress (1948) model is no longer universally accepted for mammals (Palmer, 2004; McAlpine, 2005; Palmer and Kuwada, 2005; Joris

and Yin, 2007), while it remains unchallenged in the barn owl (Wagner et al., 2007). McAlpine et al. (1996, 2001) discovered a relationship between best delay and frequency tuning in binaural neurons, which is not necessarily contradictory to the Jeffress (1948) model but certainly is not predicted by it. Moreover, the anatomical evidence for delay lines in the mammal has been questioned (Grothe, 2003). Our purpose here is to re-examine the data of Smith et al. (1993) quantitatively and to examine the anatomical data in the light of the more recently discovered relationship between ITD tuning and frequency tuning.

Materials and Methods

Material. The surgical procedure, stimulus delivery, and physiological and histological methods are described in the original study (Smith et al., 1993) and are only briefly outlined here. We will focus on the quantitative, computerized processing of the fibers labeled.

The ventral brainstem was exposed in cats of either sex, anesthetized with sodium pentobarbital. Sharp electrodes filled with either a 5% horseradish peroxidase (HRP) (type VI, Sigma) or 2% neurobiotin (Vector Laboratories) solution in 0.5 M KCl were advanced into the trapezoid body while presenting calibrated search tones. When a fiber was isolated, the excitatory ear, the characteristic frequency (CF), spontaneous activity, and threshold at CF were determined by an automated threshold tracking program. Poststimulus time histograms for short (25 ms) tones at CF were then obtained at different sound pressure levels (in 10 or 20 dB steps) usually up to 50–60 dB above threshold. Intra-axonal impalement was achieved with current pulses or electrode advancement, followed by confirmation of the physiological responses. HRP or neurobiotin was then injected by iontophoresis. After 24–36 h, a lethal dose of sodium pentobarbital was given and the animal was perfused transcardially with phosphate-buffered glutaraldehyde/paraformaldehyde fixative.

For preparation of HRP-filled axons, frozen or vibratomed 60 or 70 μm sections of the brainstem were processed using the DAB nickel–cobalt intensification method (Adams, 1981). For preparation of neurobiotin-filled cells, the sections were washed in 0.1 M phosphate buffer, incubated for 20 min in 0.5% H_2O_2, rinsed in PBS, and left overnight in phosphate buffer containing avidin-biotin-HRP reagent (ABC kit, Vector Laboratories). The sections were then rinsed in buffer, treated with DAB (as above), mounted on glass slides, counterstained with cresyl violet, and coverslipped.

Reconstructions and analysis. Because the axons typically extended over many coronal sections, detailed analysis and three-dimensional reconstructions required computer reconstruction. We used a Neurolucida system (Microbrightfield) that included an Olympus BX61 light microscope, a video camera (MBF-CX9000, Microbrightfield), a motorized stage controller (MAC5000, Ludl Electronic Products), and a personal computer. Axons were traced and digitized directly on the microscope using a UPlanFLN 40× objective. The (x,y,z) positions accompanied with axon diameter were collected every 1.9 μm on average (538 points/mm). Section thickness measured with the microscope z-axis ranged from 20 to 25 μm. Corrections were made for shrinkage along this axis (i.e., the rostrocaudal direction) according to the section thickness specified during cutting and the thickness measured in the microscope. Estimates of axon diameter were made by adjusting the diameter of a circular cursor to the width of the labeled axon and do not include the myelin sheath. For several reasons, stated in Smith et al. (1993), these measurements should be regarded as coarse estimates.

The furthest distal points that could be traced were defined as endpoints (EPs; for ease of reading we use the full words in the text and the abbreviations in figures). These points are not identical to terminals: the darkness of the label typically decreased with distance from the injection site and toward the middle of the sections, so that the finest processes could not always be followed to unambiguous terminations. Moreover, all of the reconstructions analyzed here were done with the light microscope, so we cannot be sure that the afferent endpoints terminate at a synapse. However, we have analyzed a small number of the labeled axons with the electron microscope, and the afferent terminals were confirmed to be presynaptic (Smith et al., 1991, 1993). Also, comparison with
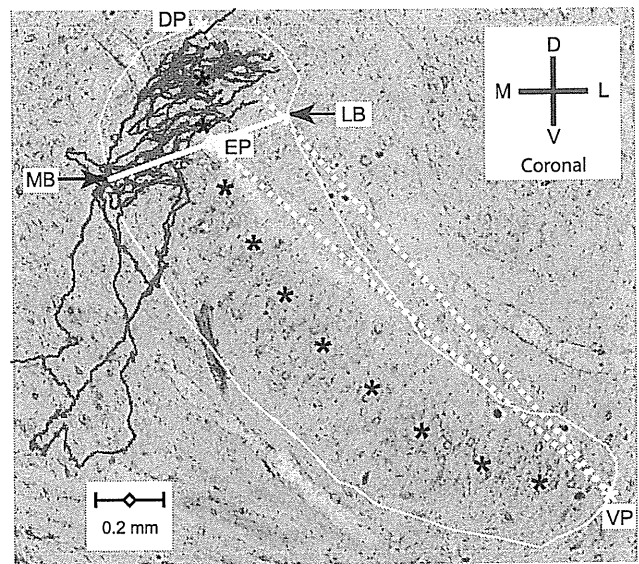

Figure 1. Illustration of measurements taken within sections. Coronal view of the contralateral projection of a traced fiber (CF, 1345 Hz) superimposed on a Nissl-stained single section, taken at the coronal level of the branch EP, indicated with the yellow dot. Yellow line, Contour of MSO on the section. Yellow asterisks, Most DP and most VP along the long axis of the MSO within the section, which is indicated with black asterisks. Drawing a line through the EP, which is approximately perpendicular to the long axis of the MSO, the arrows show the most medial and lateral points (MB and LB) of the MSO contour on this line. The two other lines (dotted white) indicate the Euclidian distances between EP and VP, and between VP and the DP of this section. Scale bar, 200 μm. Directions are indicated by the cross. D, Dorsal; V, ventral; M, medial; L, lateral.

Beckius et al. (1999) (see Results) suggests that our tracings must have covered the axons almost in their entirety in many cases. Importantly, the sheet-like mammalian MSO has limited thickness, and the delay line configuration is thought to span the rostrocaudal dimension: the main contributors to differential length are not the terminal axonal segments but rather the more proximal main stem of the axon, which gives off branches at different rostrocaudal positions (see Figs. 2C, 3). Assessment of collateral length differences along the rostrocaudal axis thus does not hinge on complete filling to the axon terminals.

We defined several markers to take measurements for numerical analysis. Figure 1 illustrates markers defined within single sections. The yellow line traces the MSO contour, and the black asterisks its long axis within the section. The yellow asterisks indicate the dorsal pole (DP) and ventral pole (VP). These are not necessarily literally the extreme dorsal and ventral points of the MSO outline in that section. For example, the ventral pole in Figure 1 is not the most ventral point of the MSO. Rather, dorsal pole and ventral pole are the extreme ends of the—often curved—long axis of the MSO within the section. The yellow disk marks one endpoint (EP). To express the dorsoventral location of an endpoint within the MSO, we measured its Euclidean distance to the ventral pole, which we normalized to the Euclidean distance between dorsal pole and ventral pole (Fig. 1, dotted white lines). Normalization facilitates comparison across animals as it reduces variance resulting from differences in absolute dimensions of the MSO. Values close to 1 indicate an endpoint located close to the dorsal pole; values close to 0 indicate a position close to the ventral pole. We also measured the mediolateral location of endpoints based on their distance to the edge of the MSO outline, taken at the intersection of the outline with a line (Fig. 1, solid white line) that is approximately orthogonal to its long axis. These intersections give two measurements for each endpoint: the medial border (MB) and the lateral border (LB). These latter measurements are inherently coarse, particularly for endpoints close to the dorsal or ventral pole of the MSO. Again, we normalized the midline (ML) position as the (Euclidian distance between endpoint and medial border)/(Euclidian distance between lat-

eral border and medial border). When this value is close to 1, the endpoint is located close to the lateral border.

Measurements taken across sections are illustrated in Figure 2 in the coronal (Fig. 2A), horizontal (Fig. 2B), and parasagittal (Fig. 2C) planes, for the same fiber used in Figure 1. First, the most rostral and most caudal sections where the MSO could be discerned are identified. The geometrical centers of the MSO outlines in these sections (Fig. 2A, green and magenta) were designated as the rostral pole (RP) and caudal pole (CP). The normalized RC distance of an endpoint relative to these poles was measured as (Euclidian distance between endpoint and rostral pole)/(Euclidian distance between caudal pole and rostral pole), illustrated with the dotted lines (Fig. 2B,C). An endpoint close to the caudal pole thus gives an RC value close to 1. For contralateral projections, we also marked the point where the axon crossed the ML. Finally, for both ipsilateral and contralateral projections we marked the first branch point (FB) (i.e., the last point of the axon that is common for all branches to the ipsilateral or contralateral MSO) (Fig. 2B,C). The axonal length from midline or first branch point to each endpoint was calculated as the sum of the distances between adjacent (x,y,z) coordinates in the course of the axon to that endpoint.

For the sake of brevity, we use the shorthand "delay line" to refer to a morphological pattern of systematic length differences in axon collaterals. We caution that the term inherently refers to a functional concept that can only be validated with physiological measurements—a point to which we will return in Discussion.

Results

The material we analyzed here consists of 14 labeled fibers, obtained from 12 animals. We reconstructed the 16 projections (9 contralateral, 7 ipsilateral) reported in Smith et al. (1993). For only two fibers (with CFs of 1498 Hz and 2470 Hz) were both contralateral and ipsilateral projections sufficiently labeled for reconstruction. A qualitative description of the course and projections of the fibers is provided in Smith et al. (1993) and is summarily illustrated here for several fibers. We identify projections with the same number, symbol, and color scheme in all figures, where relevant.

Contralateral projections

Nine contralaterally injected fibers were well labeled and used for the analyses. The axon in Figure 2 crossed the midline at a level rostral to the MSO and projected multiple collateral branches caudally before heading rostrally toward the ventral nucleus of the lateral lemniscus (VNLL). The collateral projections span approximately half of the rostral-caudal extent of the MSO nucleus with a ladder-like branching pattern that is particularly clear in the parasagittal view (Fig. 2C). Similar inner-
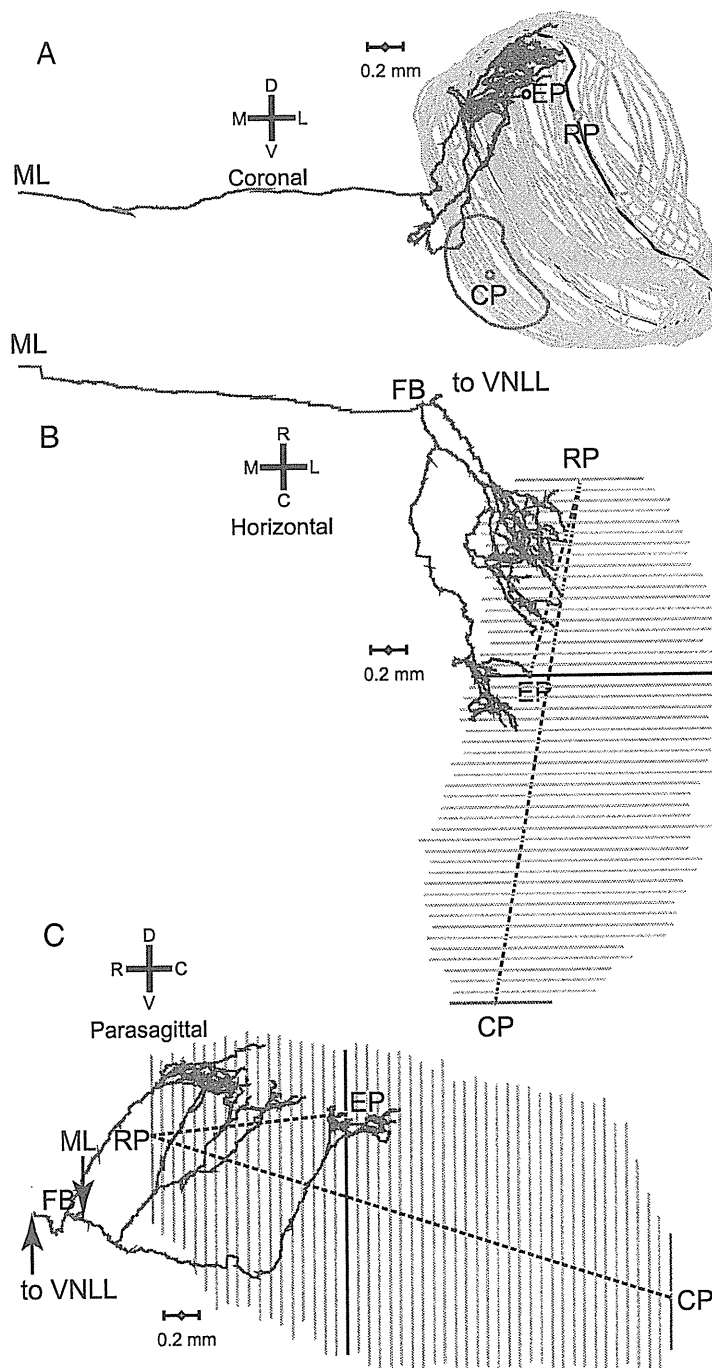

Figure 2. Example of the contralateral MSO innervation by one axon (same axon as in Fig. 1). A–C, Coronal (A), horizontal (B), and parasagittal (C) views are shown. The RP and CP were defined as the geometrical center of the most rostral (green line) and most caudal (magenta line) section, respectively. The rostrocaudal position of endpoints was quantified by measuring the Euclidian distance (dashed line) between RP and EP, and was normalized to the distance between RP and CP. The endpoint illustrated is the same one as in Figure 1; the MSO contour outlined in Figure 1 is shown in blue here. ML indicates the point at which the axon crosses the midline. CF of this fiber was 1345 Hz. A computer reconstruction of this fiber was also shown in Smith et al. (1993, their Fig. 4).

vation patterns are shown for three fibers in Figure 3. The axons in Figure 3, A and B, also cross the midline in a rostral position and give caudally directed branches over a more restricted (Fig. 3A) or less restricted (Fig. 3B) rostrocaudal distance than in Figure 2. The axon in Figure 3C, shown in horizontal view, crosses the midline at a more caudal level. It shows three branches that are directed to the central and caudal MSO, as well as one branch

eral and ipsilateral projections. Considering the branching after the first branch point, the ipsilateral projections show longer (>1 mm; see scale bar in Fig. 7A) segments than the contralateral projections before further branching. These long segments are the stems of the forward and backward branches, for example, in Figures 5 and 6. As a result, the longest distances between first branch point and endpoint are found in ipsilateral rather than in contralateral projections. Comparison of the horizontal location of the endpoints within each dendrogram indicates the range of overall length differences within projections. It is of note that this range is a few millimeters for most projections (Fig. 7A–C,F), and that the largest ranges occur in ipsilateral projections (Fig. 7D,E).

Distribution of endpoints in the parasagittal plane

Figure 8 shows the distributions of endpoints for contralateral (left column) and ipsilateral (right column) projections. Endpoints from one fiber are identified with the same colored symbol. The Figure 8 caption ranks the fibers by increasing CF. The two fibers for which both contralateral and ipsilateral projections were reconstructed are represented by the same symbols in left and right column: projections Contra 4 and Ipsi 2 (light blue inverted triangle, CF = 1498 Hz) and projections Contra 7 and Ipsi 5 (solid green triangle, CF = 2470 Hz). In all panels, the abscissa is the normalized rostrocaudal position of the endpoints,-measured as illustrated in Figure 2 (virtually identical results are obtained if the distance along the z-axis, i.e., the distance between coronal sections, is used). The ordinate of the top two panels is the normalized dorsoventral position of the endpoints, measured as illustrated in Figure 1. These two panels therefore represent a standardized side view of the MSO. As expected, the endpoint positions are orderly arranged with low-CF fibers most dorsal and high-CF fibers most ventral (this is further analyzed in Fig. 9). The endpoints of a given fiber tend to be distributed in an elongated rostrocaudal strip. This is particularly the case in contralateral projections (Fig. 8A) and less so in ipsilateral (Fig. 8B) projections, which can be elongated (projection 1), restricted (projection 7), or patchy (projection 6). In contralateral fibers, seven of the nine fibers showed a broad rostrocaudal extent, spanning 40–60% of the nucleus, but importantly none of the fibers spans the entire nucleus.

The bottom panels show the key measurement: the axonal length accumulated between the first branch point for the projection from that side, and the endpoints. For contralateral projections (Fig. 8C), this length tends to increase for endpoints positioned more caudally in the nucleus. The solid lines are linear
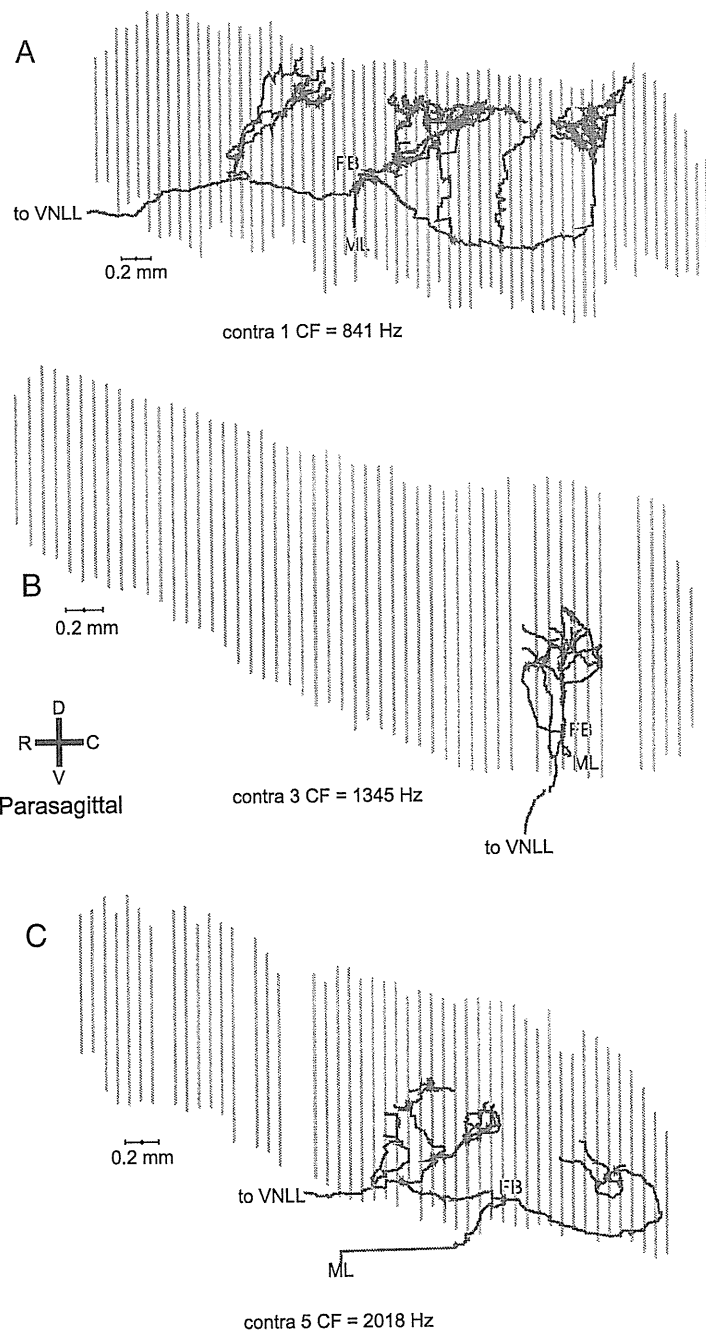

Figure 4. Parasagittal view of 3 more contralateral projections (A–C, with CFs indicated below each reconstruction) with a less clear-cut delay line configuration. In all cases, the FB is located near the center of the rostrocaudal range of EPs. The orientation shown in B applies to all panels. The color convention is as in Figure 3.

regressions; the dashed (black) line is the diagonal of equality. A "perfect" Jeffress delay line configuration would generate an endpoint distribution parallel to this line: the extra length incurred (ordinate) would equal the distance traveled rostrocaudally (abscissa). For six of nine contralateral fibers, the linear regression was significant ($p < 0.05$), with a correlation coefficient >0.80 in four of these six cases. The mean slope for the six cases was 0.91 (range, 0.54–1.65). The slope of the regression line was negative in one fiber (#3), for which the endpoints were distributed over a narrow rostrocaudal range. In two fibers (#1 and #9), the relationship was nonmonotonic, with a rostral patch of endpoints of
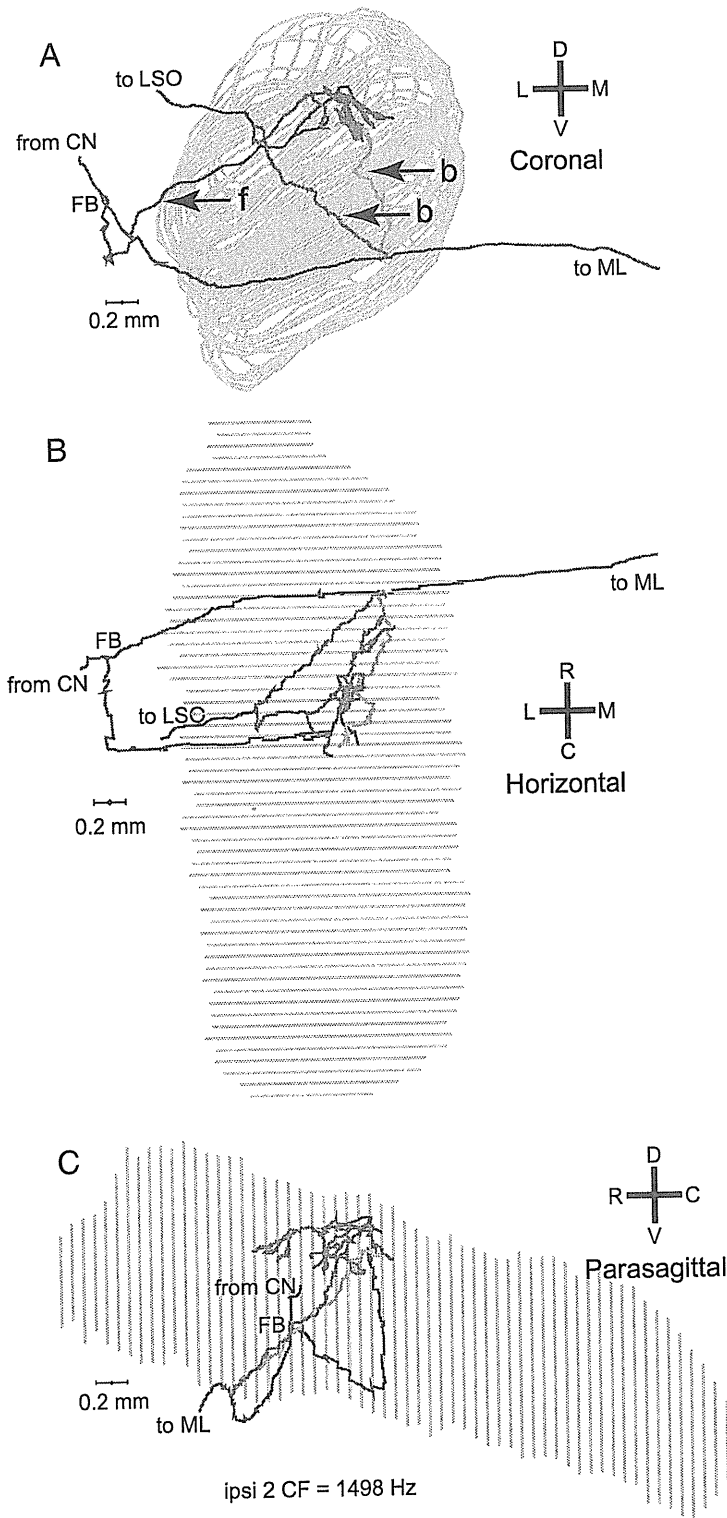
Figure 5. *A–C,* Coronal (*A*), horizontal (*B*), and parasagittal (*C*) views of a reconstructed projection of one fiber to the ipsilateral MSO. The coronal (*A*) and horizontal (*B*) views clearly show the two kinds of ipsilateral branches. One branch originates lateral to the MSO and projects forward (f, red) to it. Two branches originate after the axon has crossed the plane of the MSO and looped back (b, blue and green) to innervate the same region.

The topography of the length distributions of ipsilateral projections (Fig. 8*D*) is strikingly inhomogeneous and different from the contralateral ones. The length gradient is mostly negative (i.e., in the opposite direction than the contrateral gradient) (Fig. 8, note the difference in ordinate scale between *C* and *D*). For comparison, the negatively sloped diagonal (large dashes) is shown, which shows the slope of a perfect Jeffress delay line configuration in the direction opposite to the one dominant in contralateral fibers. Linear regressions were significant for all seven fibers ($p < 0.01$). For two fibers (#6 and #7), the number of endpoints is small. Surprisingly, the slope is positive in three fibers.

Particularly for cases where the distribution of endpoints is restricted rostrocaudally (Fig. 8*D*, fiber #7, 8*C*, fibers #3 and #4), it is questionable that the presence of a slope in the linear regressions is of functional significance. Nevertheless, overall the length gradients are in accordance with the scheme proposed by Jeffress (1948), with a majority of contralateral projections showing a rostrocaudal increase in collateral length, and a majority of ipsilateral projections showing an inverse gradient.

Interestingly, fibers tend to project to either the rostral or caudal half of the MSO, particularly on the contralateral side (Fig. 8*A,B*, with the exception of the fibers indicated by the empty red triangles). Moreover, the length gradients most consistent with a Jeffress delay configuration are found in the rostral half, both in the contralateral and in the ipsilateral branches.

Note that only the slope of the regressions is relevant to the issue of delay lines, not the vertical offset on the ordinate. This offset reflects our (arbitrary) choice of the first branch point as the point of reference for the length measurement and is affected by the absolute length of the collateral branches. A branch that is longer than the rostrocaudal MSO dimension has endpoints with ordinate values >1, as is the case for several contralateral and many ipsilateral projections. However, addition of an identical length of axon to all collateral branches (see below, Estimates of rostrocaudal axonal delay, on calculation of differences in path length between ipsilateral and contralateral projections) moves all data points of a projection up along the ordinate without affecting the presence or absence of a rostrocaudal delay.

larger length than the endpoints just caudal to it. These are fibers whose axon crosses the midline at a rather caudal position as illustrated in Figure 3*C* (fiber #9, CF = 10,508 Hz) and Figure 4*A* (fiber #1, CF = 841 Hz).

Tonotopic distribution along the dorsoventral axis

The rostrocaudal clustering of endpoints (Fig. 8*A,B*) allows us to project a map of input CFs onto the MSO. Figure 9 shows the

relationship between fiber CF and the normalized dorsoventral position of all endpoints. The endpoints contributed by one fiber are shown as a column of circles in Figure 9A, color coded for laterality. The asterisks show data points taken from the physiological data of Guinan et al. (1972, their Fig. 17). The solid circles and line show the position of the borders drawn in the summary tonotopic map of Guinan et al. (1972, their Fig. 21), at CFs of 1000, 4000, 10,000, and 20,000 Hz. There is a reasonable agreement between our data and those of Guinan et al. (1972). Much to our surprise, however, there is an upward convexity in the CF–position relationship. If low CFs were to take up a disproportionate amount of space of the MSO, relative to a logarithmic CF distribution, the relationship should be concave rather than convex: if one were to progress from dorsal MSO in a ventral direction and plot CF, there would initially be "slow" progression in CF, which would accelerate as one comes closer to the ventral pole. This is clearly not the case.

Because the cochlear map deviates from a logarithmic relationship at low CFs, we incorporate the CF–position relationship for the cochlea in the abscissa of Figure 8B, using Greenwood's equation (Liberman, 1982; Greenwood, 1990). The means and SDs of endpoint positions and the data points of Guinan et al. (1972) are replotted directly on a cochlear distance scale in Figure 9B. The data points again show an upward convexity. Predictions of the MSO CF–position relationship are now straight lines (green). The solid green line shows the relationship expected if all cochlear CFs were represented proportionally in the MSO: at low CFs, the data points tend to lie above this line. Another factor to take into account is that not all cochlear CFs appear to be represented in the MSO: the highest CF reported by Guinan et al. (1972) was 22 kHz. The dashed green line in Figure 8 shows the CF–position relationship expected if the cochlea were proportionally represented in the MSO except for its base, so that CFs >22 kHz are absent (~5 mm of the extreme base). Clearly, consideration of a limited CF representation does not alleviate the upward convexity. The prediction based on a limited CF range follows the slope of the map Guinan et al. (1972) reasonably well, but again the representation of the cochlear apex is compressed for our data, with the majority of low-CF data points lying above the dashed line.

The MSO tends to show curvature in the coronal plane (Figs. 1, 2, 6), and this curvature can be more pronounced at the dorsal
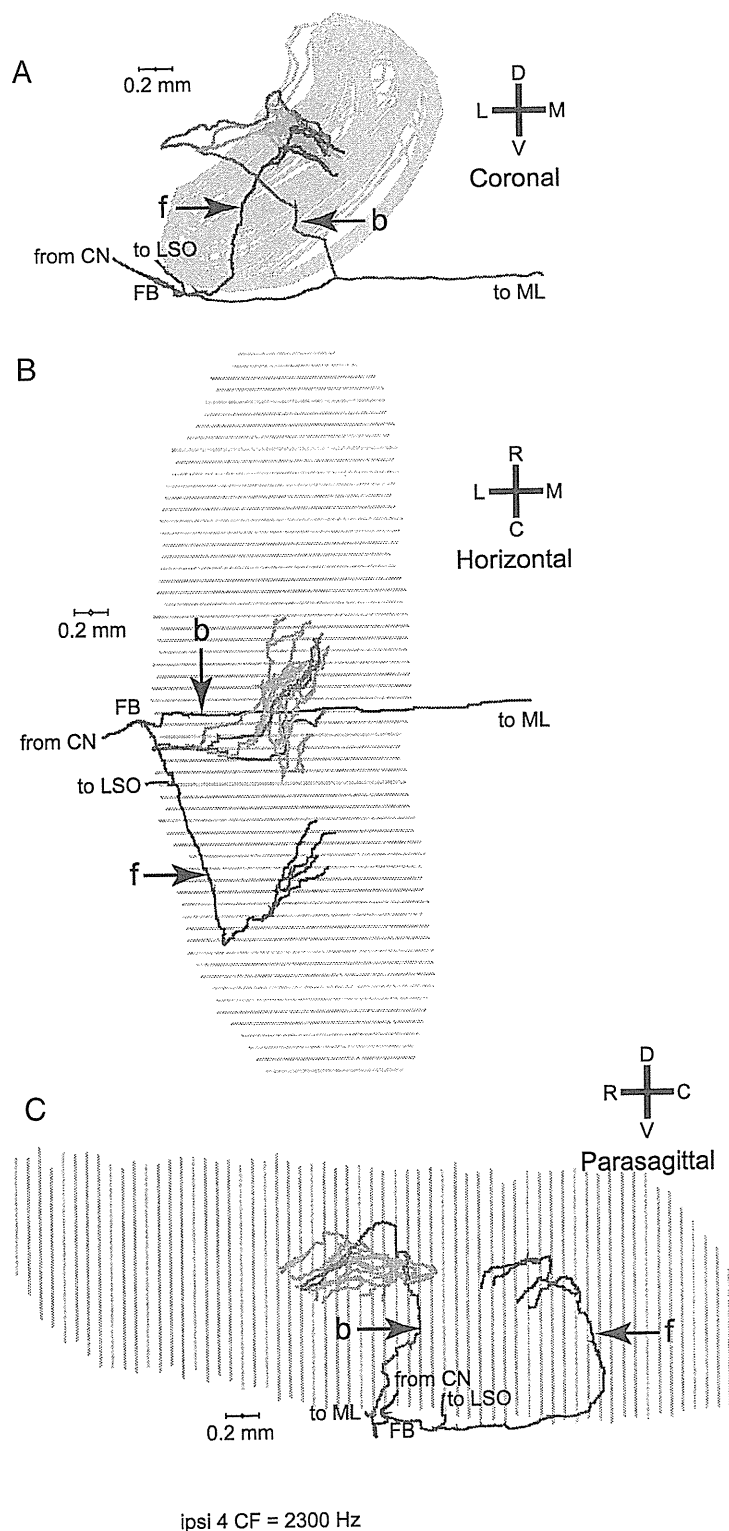

Figure 6. Another example of an ipsilateral MSO projections of one fiber. *A*, This fiber ran underneath the MSO (coronal view) and also formed forward (f) and backward (b) projecting branches. *B*, *C*, The horizontal (*B*) and parasagittal (*C*) views reveal that the branches innervate different rostrocaudal portions of the MSO. The backward branches (green and blue) innervated a more rostral portion of the MSO and covered more length of axon from FB than the forward branches.

pole (Fig. 1). Because our measure of dorsoventral location does not take curvature into account, we recalculated the dorsoventral positions in Figures 8, 9, and 10 taking the Euclidean distance of the endpoint to the ventral pole (as before), but now normalized
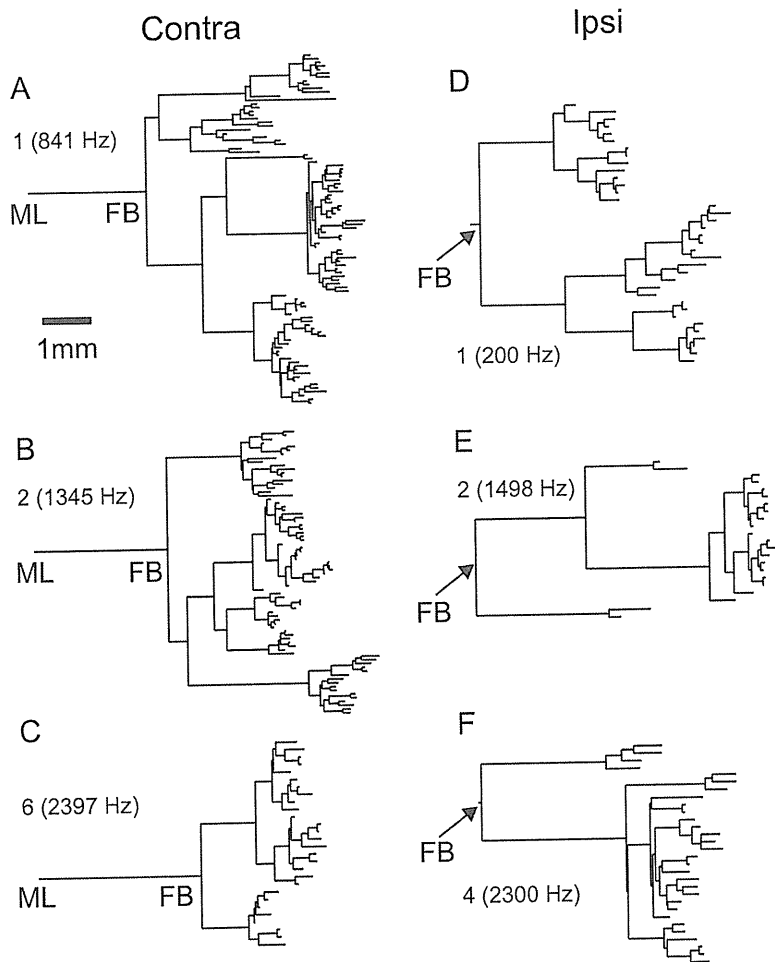
Contra

A

1 (841 Hz)

ML   FB

1mm

B

2 (1345 Hz)

ML   FB

C

6 (2397 Hz)

ML   FB

Ipsi

D

FB

1 (200 Hz)

E

2 (1498 Hz)

FB

F

FB

4 (2300 Hz)

Figure 7. *A, B,* Dendrograms showing the branching pattern and length of axonal segments for three contralateral (*A*) and three ipsilateral projections (*B*). The scale bar in *A* applies to *A–F.* The horizontal dimension represents the axonal length of branch segments; the vertical dimension is only used to offset these segments and has no meaning with regard to length or order. Fiber number and CF are indicated for each projection. Cross-linking to previous figures with computerized reconstructions is as follows: *A* = Figure 4*A;* *B* = Figures 1 and 2; *C* = Figure 3*A; D* = Figure 5 of Smith et al. (1993); *E* = Figure 5; *F* = Figure 6.

fibers showing forward branches (Fig. 10 legend, + symbols), these branches give endpoints located more lateral than the backward branches (projections 2, 4, and 6).

Axon diameter and conduction velocity
The analysis so far has concerned branching patterns, endpoint position, and axon length. Other factors than axonal length contribute to the time delay in action potential propagation; most importantly myelination, axon diameter, and internodal distance. The only additional factor we can assess in our material is axon diameter, be it only crudely for the various reasons pointed out in Smith et al. (1993). Diameters were measured at each axonal (*x,y,z*) position entered. Using these measurements, we calculated the mean diameter of each "segment," which is the part of an axon between neighboring branch points; branch points and endpoints; or midline and branch point. Figure 11 shows the mean diameter as a function of distance from the midline (Fig. 11*A*) for contralateral projections, and from the first branch point (Fig. 11*B*) for ipsilateral projections. These graphs are obtained by moving from left to right across the dendrograms (Fig. 7), and tallying and averaging all the segment diameters that are present for a given length from the starting point (Figs. 2–4, ML, 5, 6, FB). Close to the starting points, the mean diameter jumps in large steps because few branches are present, but the trace becomes smoother as more branching occurs. There is a general decrease in axon diameter toward the endpoints.

To compare diameters of contralateral and ipsilateral branches, we first determined the number of segments of a given diameter (bin size, 0.1 μm). Dividing by the number of contributing fibers (9 for contralateral and 7 for ipsilateral projections), we obtain the average numbers shown in Figure 12, *A* and *B.* The diameters are largely between 1 and 3 μm; the mean is 1.8 μm for both distributions (*t* test, *p* = 0.27). For the contralateral projections, the axonal segments include all segments of projections into the contralateral MSO arising after the midline crossing, while for the ipsilateral projections they include all segments projecting into the ipsilateral MSO after the first branch point. The reason that we included the "extra" segment between midline and first branch point in the contralateral projections is that the midline gives an "absolute" reference that can be identified in each animal, which allows an estimate of path length for the axon in the contralateral hemibrain. These proximal segments are shown in black in Figure 12, *A* and *C.* Removal of these segments did not affect the lack of a statistically significant difference between the diameter distributions of contralateral and ipsilateral projections (*p* = 0.13).

Numerically, the final segments, shown in gray in Figure 12, dominate the histograms, due to the profuse branching once the collaterals reach the tonotopic layers where they form their endpoints. Because the axons progressively taper (Fig. 11) and much

to the sum of the distance of the endpoint to the ventral and dorsal poles (i.e., the normalization was now to the sum of the line segments EP–VP and EP–DP). This recalculation caused only minor shifts in ordinate position and did not remove the bias of low-CF data points above the green lines in Figure 9*A,B.*

Distribution of endpoints in the mediolateral dimension
Figure 10 shows the normalized mediolateral versus dorsoventral distribution of endpoints. As commented on in Materials, determination of the mediolateral endpoint position is inherently inaccurate. Relative to its small width, the medial and lateral border of the MSO cannot be determined with much precision (note that, on the square axes of Fig. 10, the mediolateral dimension is much magnified relative to the dorsoventral dimension, approximately by a factor 3.6). The uncertainty becomes particularly large for endpoints located close to the dorsal or ventral pole. This is visible in Figure 10: the mediolateral spread of points increases toward the dorsal pole. Nevertheless, as expected (Stotler, 1953), the contralateral endpoints occupy dominantly a medial position, and the ipsilateral endpoints a lateral position. Of interest is that the forward and backward branches of the ipsilateral projection seem to occupy the same dorsoventral (tonotopic) but not mediolateral position. For the four

of the delay must accrue at the distal branches, it is of interest to compare contralateral and ipsilateral distributions for the final segments. Again, there is no difference in the distributions for contralateral and ipsilateral fibers ($p = 0.26$).

Next, to visualize the relationship between diameter and length of segments, we summed the lengths for all segments with a given diameter for all fibers (bin size 0.1 μm) and normalized to the number of contributing fibers (9 for contralateral and 7 for ipsilateral projections). Thus, Figure 12, C and D, shows average segment length of a given diameter for contralateral and ipsilateral projections, respectively. Statistical comparison shows that at none of the bins for which both contralateral and ipsilateral values are present is there a significant difference in segment length (t test, $p > 0.05$).

From the axon diameter and length, estimates for conduction speed and time can be calculated. We followed the method of Beckius et al. (1999) to estimate conduction time as follows:

$$L/(d^*RV), \qquad (1)$$

with L being the length (in millimeters) of axon between two branch points, d being the average diameter (in micrometers) of that segment, and RV being an experimentally derived constant (9.167 mm/ms/μm) (Waxman and Bennett, 1972). For each endpoint, the conduction times of all segments interposed between that endpoint and a fixed starting point were added.

In Figure 13 we show the estimated conduction times for all endpoints using as starting points the midline (Fig. 13C, contralateral projections) or the first branch point (Fig. 13D, ipsilateral projections) against the length of axon traversed to reach these endpoints. The relationship is very orderly; in all fibers, linear regression (data not shown) of length on conduction time was significant ($p < 0.001$; $p < 0.01$ in one fiber). This result is not surprising and may seem trivial because of the proportionality of estimated conduction time to length in Equation 1. However, if the average diameter to reach one endpoint were larger than that to reach another endpoint of the same tree, the conduction time would be shorter even if the average length were the same (Fig. 13A). Likewise, there could be a length difference that is compensated by a difference in axon diameter (Fig. 13B). The linear distributions of endpoints in Figure 13, C and D, show that d (Eq. 1) is "well behaved" in the sense that diameter decreases similarly with distance in all branches and that there is no systematic effect of diameter that offsets or enhances the "delay line effect" of the branching pattern. The slope of the linear regressions (data not shown) was on average 19.3 m/s for the contralateral and 17.9 m/s for the ipsilateral projections (ranges: 14–26 m/s for Contra; 13–21 m/s for Ipsi).

Contra
▲ 1 (841 Hz)
▽ 2 (1345 Hz)
▲ 3 (1345 Hz)
▽ 4 (1498 Hz)
△ 5 (2018 Hz)
▽ 6 (2397 Hz)
△ 7 (2470 Hz)
▽ 8 (7184 Hz)
▲ 9 (10508 Hz)

Ipsi
▲ 1 (200 Hz)
▽ 2 (1498 Hz)
△ 3 (1903 Hz)
▽ 4 (2300 Hz)
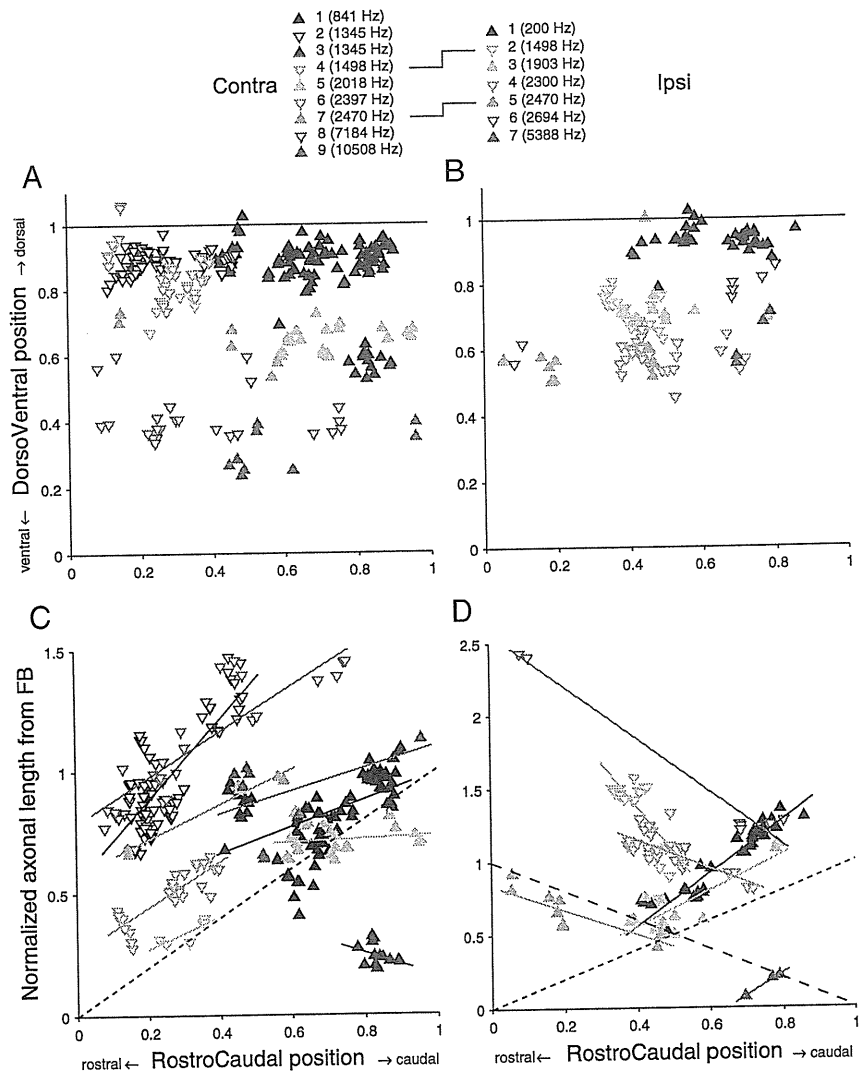△ 5 (2470 Hz)
▽ 6 (2694 Hz)
▲ 7 (5388 Hz)

Figure 8. Length gradients along the rostrocaudal axis of the MSO. *A, B,* Distribution of endpoints of contralateral (*A*) and ipsilateral (*B*) projections on normalized MSO axes. *C, D,* Axonal length from FB to the different endpoints. Solid lines are linear regressions. The diagonals with short dashed lines indicate the diagonal of equality; the diagonal with the long dashed lines indicates the slope expected for an opposite length gradient. The caption shows the symbols and color used for the endpoints originating from the different fibers, numbered for increasing CF and reused in subsequent figures. The lines between left and right symbol captions indicate the two fibers for which both the contralateral and ipsilateral projections were reconstructed.

Note that these slopes do not give conduction speeds, but rather the speed at which excitation would "sweep" through the endpoints. If all endpoints were arranged in an orderly fashion as in Jeffress' model so that the endpoints with the shortest axonal length were located (e.g., most rostrally and those with the longest length most caudally), the range of conduction times spanned by the endpoints of one axon would equal the range of its x-values in Figure 13, C and D [e.g., 220–350 μs for the contralateral projection (#1), represented by the black triangles in C; i.e., a range of 130 μs]. However, as already shown in Figure 8, C and D, the arrangement of endpoints is not that orderly. Again taking projection #1 as an example, it can be seen in Figure 8C that endpoints with similar axonal length occur over a significant rostrocaudal range. We return to this point in the section below, Estimates of rostrocaudal axonal delay (Fig. 14).

The lines in Figure 13, C and D, connect starting points, branch points, and endpoints of each projection. The slope of each line equals the speed of the corresponding segment. This
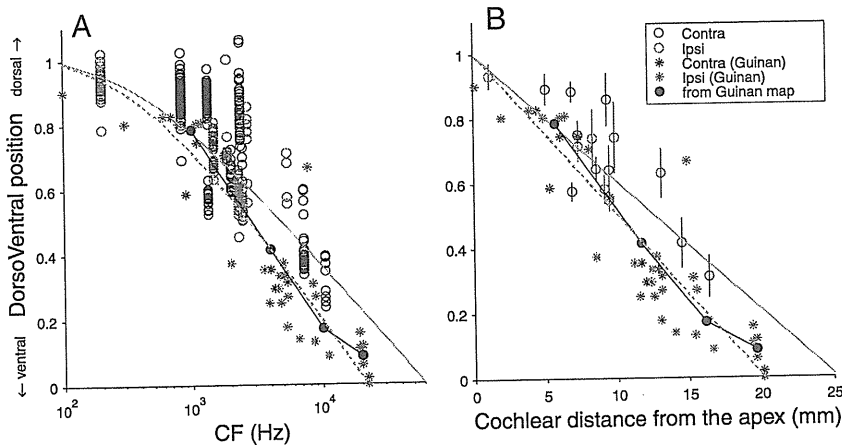
Figure 9. Tonotopic compression of low frequencies in MSO. *A, B,* The dorsoventral location, normalized to the dorsoventral extent of the MSO, is shown for all endpoints of all reconstructed fibers on a logarithmic CF abscissa (*A*) and for their mean and SD on a cochlear distance abscissa (*B*). Each circle in *A* indicates a single endpoint (blue, contralateral fiber; red, ipsilateral fiber). The asterisks and the black circles and line show extracellular and summary data from Guinan et al. (1972) (see main text). The green lines are predicted relationships based on the cochlear tonotopic map, based on Greenwood's formula (Greenwood, 1990). The solid green line is the prediction for a full representation of all CFs; the dashed line is for a representation limited to ≤22 kHz. The endpoints at low CFs cluster above the green lines. If low CFs were over-represented in MSO, those endpoints would be expected to cluster below rather than above the green lines.
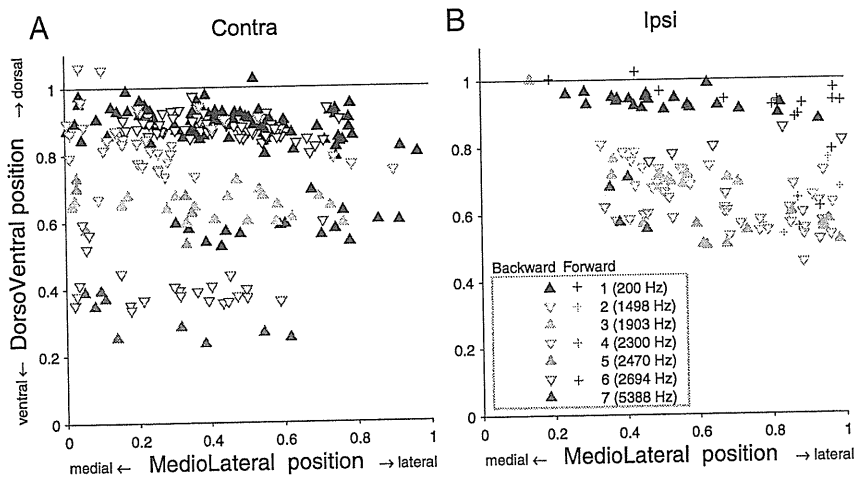

Figure 10. *A, B,* Distribution of endpoints in the coronal plane, for contralateral (*A*) and ipsilateral (*B*) projections. Symbol use for *A* is as in Figure 8. The "Backward" and "Forward" in *B* refer to backward and forward branches, as illustrated in Figures 5 and 6.

the large diameter of that segment (Fig. 11*A*), while the ipsilateral projection tends to sustain long (Fig. 7*E,F*) and large-diameter (Fig. 11*B*) forward and backward segments after the first branch point. In summary, the overall distribution of axon diameter and its progression along the axon is similar in contralateral and ipsilateral projections.

Estimates of rostrocaudal axonal delay

The main quantitative check so far regarding Jeffress' (1948) hypothesized axonal delay lines was in Figure 8, *C* and *D*, which examined length as a function of rostrocaudal position. In a similar format, Figure 14, *A* and *B*, replots the data directly in dimensions of time and space: estimated conduction time, calculated from both diameter and length, versus rostrocaudal position in micrometers from the most rostral MSO section. The abscissa origin coincides with the section containing the rostral pole, while the location of the section of the caudal pole is indicated by an asterisk at the caudal end of a linear regression line drawn through all the endpoints of each projection. As expected from the general trend of a graded decrease in axon diameter (Figs. 11–13), the relationships of Figure 8, *C* and *D*, are preserved in Figure 14, *A* and *B*. Thus, it does not appear to be the case that afferent branch diameter is regulated to fine tune delay lines based on length, at least not at the level of assessment of diameter that is possible with our material.

To summarize the regression data on estimated conduction times (Fig. 14*A,B*) and measured length gradients (Fig. 8*C,D*), Figure 14*C* shows the slopes of the linear regressions in these figures. Abscissa values of 1 and −1 indicate "perfect" slopes of delay, where the extra length of axon is identical to the extra distance in rostrocaudal (or caudorostral) direction (Fig. 8, compare diagonals in *C* and *D*). All significant (large symbols) contralateral projections, as well as three ipsilateral projections, contribute data to the upper right quadrant. The data points in the lower left quadrant consist only of ipsilateral projections, which form a length gradient in the caudorostral direction. Note that the most extreme positive and negative values are found in the ipsilateral projections. Also of note are the rather modest values of the estimated delays. To map the physiological range of delays (300–400 μs in the cat) (Roth et al., 1980) on the length of MSO (3–4 mm) (Fig. 14*A,B*), the interaural delay accrued per millimeter should be ~100 μs. The ordinate values in Figure 14*C* show that the estimated "monaural" delays fall short for the contralateral projections. The ipsilateral delays come close but are in the wrong direction for the positive values, and for the negative values some of the projections are limited in spatial extent (Fig. 14*B*). In Jeffress' (1948) scheme, it is the combination of ipsilateral and con-

slope decreases with increasing distance from the starting point, due to the gradual decrease in axon diameter, and gives rise to the general curvature in the data. For each endpoint, the length traversed divided by the estimated conduction time gives an estimate of the average speed from starting point to each endpoint (this speed equals the slope of a line connecting the endpoint to the origin in Fig. 13*C,D,* illustrated for the diagrams in Fig. 13*A,B* with dashed lines). The ranges of estimated speeds are shown in Fig. 13*E–G.* They are similar across endpoints and CFs, and are also very similar for contralateral and ipsilateral fibers (means, 20.1 and 19.3 m/s, respectively), when taking midline (Fig. 13*E*) and first branch point (Fig. 13*G*), respectively, as a starting point. When the contralateral side is also referenced to the first branch point rather than to the midline (Fig. 13*F*), the estimated conduction speed drops to 18.4 ms/s on average. This reflects the long distance (several millimeters) of the segment from midline to first branch point in contralateral fibers (Figs. 7*A–C,* 11*A*) and